Drivers of diurnal and seasonal dynamics of triple oxygen isotopes in atmospheric water vapor and precipitation at a Mediterranean forest site

Claudia Voigt[1,a], Christine Vallet-Coulomb[1], Clément Piel[2], Joana Sauze[2], Ilja M. Reiter[3], Jean-Philippe Orts[4], Françoise Chalié[1], Christophe Cassou[5], Irène Xueref-Remy[4], Anne Alexandre[1]

[1]Aix-Marseille University, CNRS, IRD, INRAE, CEREGE, 13545 Aix-en-Provence, France
[2]ECOTRON Européen de Montpellier, UAR 3248, Montpellier University, CNRS, 34980 Montferrier-sur-Lez, France
[3]Research Federation ECCOREV, FR3098, CNRS, 13545 Aix-en-Provence, France
[4]IMBE, CNRS, University of Avignon, Aix-Marseille University, IRD, 13397 Marseille, France
[5]CECI, Université de Toulouse, Cerfacs, CNRS, Toulouse, France
[a]present address: Institute of Soil Sciences and Site Ecology, TU Dresden, 01737 Tharandt, Germany

Correspondence to: Claudia Voigt (claudia.voigt@tu-dresden.de)

Abstract.

Triple oxygen isotopes are powerful to trace hydrological processes, yet their variability in atmospheric water vapor and the underlying controls remain poorly understood. We present a one-year record of triple oxygen and hydrogen isotopes of atmospheric water vapor ($\delta^{18}O_V$, d-excess$_V$, ^{17}O-excess$_V$) measured below, within and above a downy oak forest canopy at the AnaEE platform O_3HP in the French Mediterranean. This vapor dataset is complemented by isotopic data of precipitation ($\delta^{18}O_P$, d-excess$_P$, ^{17}O-excess$_P$) and groundwater, as well as monthly observations of stomatal conductance and transpiration. Seasonal variations in ^{17}O-excess$_V$ and d-excess$_V$ likely reflect changing evaporative conditions at oceanic moisture sources. d-excess$_P$ and ^{17}O-excess$_P$ show a same seasonal pattern, enhanced by summer rain re-evaporation. However, no clear isotopic differences were observed in vapor or precipitation derived from different oceanic source regions and weather regimes, likely due to frequent mixing of multiple moisture sources. Diurnal variations in ^{17}O-excess$_V$ and d-excess$_V$ reflect a combination of vegetation-related processes, including local evapotranspiration. However, diurnal variations largely offset each other at the daily scale. Although precipitation often deviates from isotopic equilibrium with near-surface atmospheric water vapor at the event scale due to incomplete equilibration and rain re-evaporation, equilibrium water vapor reliably approximates the near-surface isotopic composition of atmospheric water vapor at annual scale. Our results highlight the potential of ^{17}O-excess for understanding water exchange between the land and the atmosphere, regardless of climatic and vegetation conditions. They enhance the mechanistic interpretation of precipitation isotopes, which is essential for reliable paleoclimate reconstructions.

1 Introduction

The analysis of triple oxygen isotopes (^{16}O, ^{17}O, ^{18}O) has become an important tool in the study of the hydrological cycle. The secondarily derived ^{17}O-excess parameter [$= \delta'^{17}O - 0.528\ \delta'^{18}O$, with $\delta' = \ln(\delta + 1)$] complements the traditional d-excess [$= \delta^2H - 8\ \delta^{18}O$] in the assessment of hydrological processes. In contrast to d-excess, ^{17}O-excess is only weakly affected by temperature (Barkan & Luz, 2005) and, therefore, insignificantly influenced by condensation and Rayleigh distillation during rainout (Xia et al., 2023). Hence, variations of ^{17}O-excess are mainly driven by diffusive fractionation processes that make it a valuable tracer for climate conditions during evaporation, mainly atmospheric relative humidity (RH) (Alexandre et al., 2018, 2019; Gázquez et al., 2018, 2023; Outrequin et al., 2021; Surma et al., 2015, 2018). Moreover, the ^{17}O-excess of surface waters can be used for identifying if a lake receives continuous surface or subsurface inflow (Surma et al., 2015, 2018), mixing processes between evaporated and unevaporated waters (Voigt et al., 2021), quantifying lake hydrological balance (Pierchala et al., 2021; Voigt et al., 2024) and tracing water exchange at the soil-plant-atmosphere interface (Landais et al., 2006; Li et al., 2017; Voigt et al., 2023). However, little is known about the variability of ^{17}O-excess in atmospheric water vapor and the processes driving it.

Comprehensive knowledge of these processes is essential for constraining the water cycle at the soil-plant-atmosphere interface and for isotope-enabled hydrological modeling. So far, measurements of ^{17}O-excess in atmospheric water vapor have been restricted to discrete samples collected by cryogenic distillation and limited to a handful of studies. Data from atmospheric water vapor over the Southern Ocean (Uemura et al., 2010), continental atmospheric water vapor over northern Greenland (Landais et al., 2012) and a tropical island (Uechi and Uemura, 2019) suggest the potential of ^{17}O-excess to trace changes in relative humidity at the oceanic moisture sources. However, mixing of air masses from different sources, terrestrial moisture recycling, raindrop re-evaporation and local sublimation can alter ^{17}O-excess of continental atmospheric water vapor and associated precipitation (Arellano et al., 2024; Aron et al., 2021; Giménez et al., 2021; S. He et al., 2021; Landais et al., 2010, 2012; Liang et al., 2024; Ranjan et al., 2021; Surma et al., 2021; Voarintsoa, 2025; Zhang et al., 2025). The respective impact of these processes, inherent to the water cycle, on the ^{17}O-excess and d-excess of precipitation has been recently theorized by Xia et al. (2023). In addition, under certain conditions, stratospheric intrusions can significantly increase the ^{17}O-excess of atmospheric water vapor (Lin et al., 2013).

Here, we quantify the variability in ^{17}O-excess of atmospheric water vapor and precipitation in a French Mediterranean forest ecosystem across seasonal, monthly and daily scales, and assess its key driving processes. The triple oxygen and hydrogen isotopic composition of atmospheric water vapor ($\delta^{17}O$, $\delta^{18}O$, δ^2H, ^{17}O-excess and d-excess) was continuously measured over one year using a cavity ring-down spectrometer (CRDS) at multiple heights – below, within and above a deciduous Mediterranean oak forest canopy. Additionally, we analyzed the triple oxygen and hydrogen isotopic composition of precipitation samples collected at quasi-event scale over the sampling period. Meteorological parameters and vegetation phenology, stomatal conductance and transpiration were monitored throughout the oak forest's growing season (live foliage). We quantified oceanic moisture sources and associated evaporative conditions over the ocean and identified eight synoptic

patterns that describe synoptic atmospheric variability over the course of the year. We discuss key processes that control the triple oxygen isotopic variability of atmospheric water vapor and precipitation across timescales at the study site. We further examine the hypothesis of isotopic equilibrium between atmospheric water vapor and precipitation, which is often used in surface iso-hydrological models (e.g., Arnault et al., 2021).

2 Materials and Methods

2.1 Study site, meteorological and vegetation measurements

The AnaEE (European Research Infrastructure 'Analyses and Experimentation on Ecosystems') *in natura* facility O_3HP (Oak Observatory of the Upper-Provence Observatory) is situated in a deciduous Mediterranean forest about 70 km inland, north of Marseille (France) at an altitude of 680 m above sea level (43.935° N, 5.711° E, Fig. 1a). The forest is dominated by downy oak (*Quercus pubescens* Willd.) with co-dominant Montpellier maple (*Acer monspessulanum* L., 25% of canopy leaf mass). The tree canopy height is between 2 m and 6 m. In the understory, typical sub-Mediterranean grasses, forbs, and shrubs are present. In 2021, the stand density was about 3550 trees per hectare with a stand basal area 18.8 m^2 ha^{-1}, an average leaf area index of about 2 m^2 m^{-2}, ranging between 1 and 3 m^2 m^{-2}, and a canopy gap fraction of about 25% (LAI-2000, LI-COR Inc., Nebraska, USA). In February 2021, a 5.5 m^2 plot of the C3 grass species *Festuca arundinacea* Schreb. was set up in the understory of the forest (Voigt et al., 2023).

The following climate parameters were measured on the experimental site: global solar radiation at 6 m above ground (LI-200, LI-COR Biosciences Inc., Nebraska, USA), precipitation amount (15189 H, LAMBRECHT meteo GmbH, Göttingen, Germany), RH and atmospheric temperature (T_{air}) at 0.6 m height next to the grass plot and at 1.5 m, 1.9 m, 4.4 m and 6.15 m height in the oak forest canopy (HMP155, Vaisala Oyj, Vantaa, Finland). Furthermore, we used RH and wind speed measured at 10 m height and T_{air} measured at 10 m, 50 m and 100 m height on the on-site ICOS Tower. Each parameter was extracted in hourly resolution from the COOPERATE database (Reiter et al., 2015).

Photos of the forest canopy were taken every day from a fixed point to provide information on the oak phenology. Stomatal conductance (g_s) and transpiration were continuously measured on a single oak leaf in the sun-crown of the canopy using a gas exchange system (Li-6400 XT, LI-COR Inc., Nebraska, USA) over 24 hours in the early, middle and last stage of the oak growing season (on June 22-23, August 27-28 and October 22-23, respectively). Simultaneously, the spatial variability of g_s, was assessed by hourly g_s measurements on the abaxial side of 18 oak leaves in the shade- and sun-crown of six different trees (i.e. 3 leaves per tree), using a porometer (AP4, Delta-T Devices LTD, Cambridge, UK).

2.2 Isotopic monitoring of groundwater, precipitation and atmospheric water vapor

All isotopic data presented herein are expressed in delta-notation and normalized on the Vienna Standard Mean Ocean Water – Standard Light Antarctic Precipitation (VSMOW-SLAP) scale. Throughout this study, δ-values, δ′-values, and d-excess are

reported in per mil (10^{-3}, ‰), while ^{17}O-excess is reported in per meg (i.e., 0.001‰). The isotopic compositions of atmospheric water vapor and precipitation are denoted by the subscripts V and P, respectively.

Figure 1 illustrates the experimental setup for *in-situ* isotopic monitoring of atmospheric water vapor. The inlets of four 1/4-inch wide PFA tubes (PFA-T4-062-100, Swagelok, Ohio, US) were positioned at 0.4 m above the grass plot, and at 1.5 m, 3.5 m, and 12.5 m above ground level (agl) – below, within and above the downy oak forest canopy, respectively. From bottom to top, the tubes were approximately of 11.5 m, 15 m, 20 m, and 32 m length. The tubes were continuously pumped at a flow rate of ~5 L min^{-1} using oil-free diaphragm pumps. Along the entire length, the tubing was insulated and heated to 40–50°C using self-regulating heat wire to prevent condensation. A funnel covered by a net was placed at each inlet for protection from rain and suction of insects and large aerosol particles. A split of each line was passed to a 16-Port Distribution Manifold (A0311; Picarro Inc., California, USA) coupled to a high-precision vaporizer (A0211, Picarro Inc., California, USA) and a CRDS (L2140-i; Picarro Inc., California, USA). The instrument was installed in an air-conditioned building on the experimental site and was operated in ^{17}O Dual Liquid/Vapor mode. It subsampled air from a selected tube with a flow rate of about 35 mL min^{-1} for 70 minutes before switching to the next tube. During data processing, the first 10 minutes of each line measurement were discarded to minimize memory effects, and the subsequent 60 minutes were averaged. Such long integration times were necessary to achieve high precision in ^{17}O-excess (see below). From January to May 2021, measurements were alternated between the two tubes positioned at 0.4 m above the grass plot and 12.5 m above the forest canopy, resulting in 9–10 measurements per height and day. From June to December 2021, measurements were alternated between all four heights, resulting in 4–5 measurements per height and day.

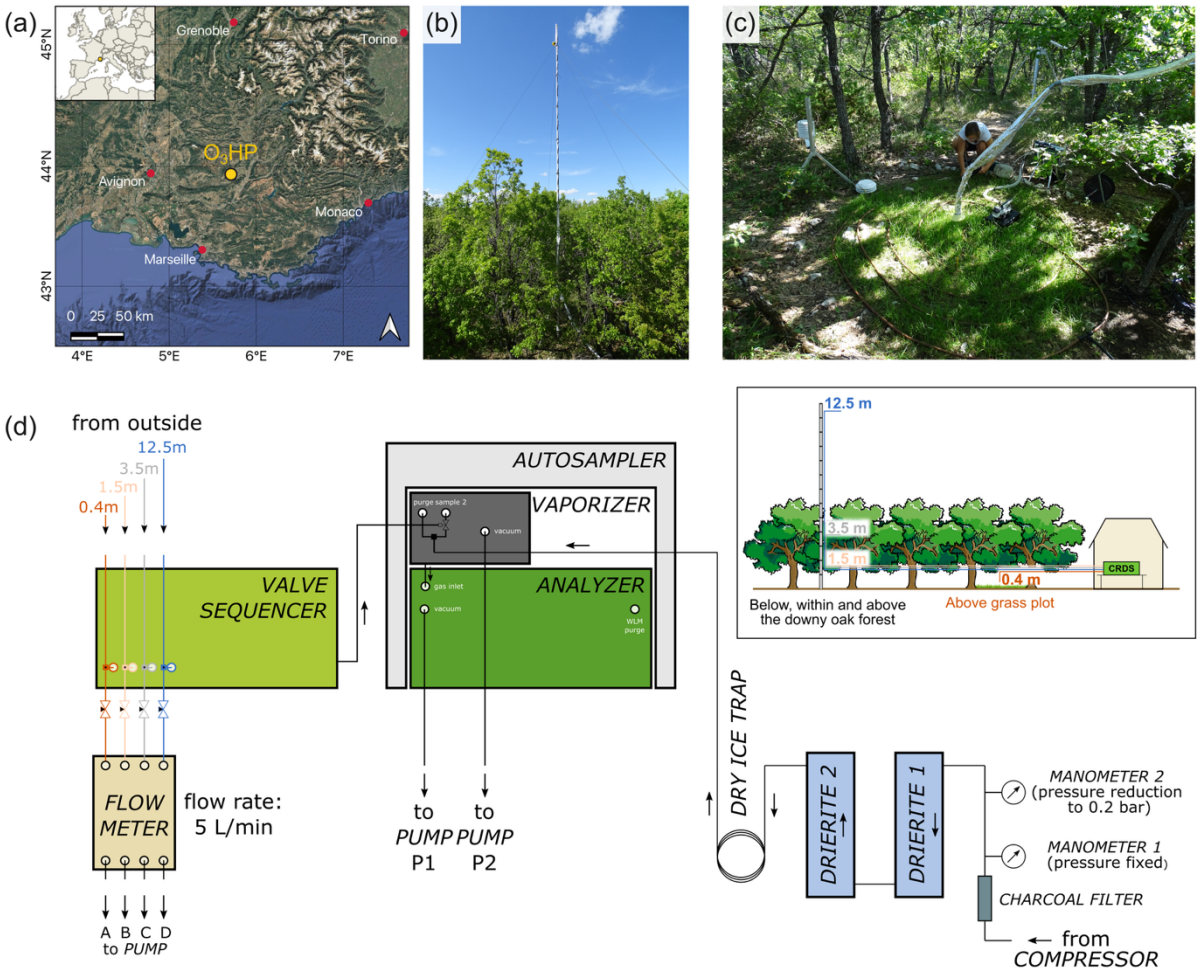

Figure 1: (a) Location of the study site *O_3HP*. (Map: Google ©2026, Data: SIO, NOAA, U.S. Navy, NGA, GEBCO, Image: Landsat / Copernicus), (b) Mast installed within the downy oak forest canopy, equipped with intake lines for continuous atmospheric water vapor isotopic sampling. (Photo: C. Voigt). (c) Grass plot in the forest understory instrumented with micro-climate and atmospheric isotopic measurement systems (Photo: A. Alexandre). (d) Schematic illustration of the experimental setup. The solenoid valve behind the vaporizer allowed switching between the valve sequencer used for atmospheric water vapor measurements and the dry air stream provided by the combination of compressed air, drierite columns and the dry ice trap used for weekly calibrations. See text for detailed description.

The calibration protocol of atmospheric water vapor isotopic data is described in detail in Voigt et al. (2023). Three liquid water standards that covered the expected isotopic range of atmospheric water vapor at the study site were analyzed weekly using an autosampler system (A0325, Picarro Inc., California, USA) coupled to the high-precision vaporizer and the analyzer (Fig. 1). The liquid standards were injected in a dry air stream, produced by a lubricated mobile air compressor (MONTECARLO FC2, ABAC air compressors, Italy) and further dried using two drierite columns and a dry ice trap. Using dry ambient air instead of synthetic air as carrier gas for calibration of atmospheric water vapor isotopic measurements is crucial to avoid any potential matrix effect (Voigt et al., 2022). From January to May, standards were analyzed at four water

mixing ratios (3000 ppmv, 7000 ppmv, 11000 ppmv and 17000 ppmv) to assess temporal variability of the mixing ratio dependency. As no significant variation was observed, measurements from June to November were conducted only at 11000 ppmv for VSMOW-SLAP normalization. The mixing ratio dependency functions for the three liquid standards were determined based on three higher-resolved water mixing ratio dependency assessments performed in May 2021, October 2021 and January 2022. From the end of November to December, standards were additionally analyzed at 5000 ppmv as atmospheric water mixing ratios were low. For details on the run architectures see Table A1.

For calibration, raw $\delta^{17}O$, $\delta^{18}O$ and $\delta^{2}H$ of the liquid standards from four consecutive runs (four weeks) were averaged and subsequently corrected to the water mixing ratio of the measured atmospheric water vapor:

$$\delta_{\mathrm{std,corr}} = \delta_{\mathrm{std,meas}} + a\left(\frac{1}{H_2O_{\mathrm{atm}}} - \frac{1}{H_2O_{\mathrm{std}}}\right) + b(H_2O_{\mathrm{atm}} - H_2O_{\mathrm{std}}) + c \qquad (1)$$

where δ denotes $\delta^{17}O$, $\delta^{18}O$ or $\delta^{2}H$ (in ‰), and H_2O is the measured water mixing ratio (in ppmv) of the standard (std) and the atmosphere (atm), respectively. The coefficients a, b and c describe the mixing ratio dependency functions and are specific for $\delta^{17}O$, $\delta^{18}O$ and $\delta^{2}H$ and for each standard (Table A2). The mixing ratio corrected values of the standards with the lowest and the highest isotopic values were then used for two-point calibration on VSMOW-SLAP scale, while the third standard with an intermediate isotopic composition served as quality control.

The precision of raw isotopic data was estimated from Allan deviation analysis of 24-hour *in-situ* measurements of atmospheric water vapor at O_3HP in June 2021. While the optimal integration time for $\delta^{17}O$, $\delta^{18}O$, $\delta^{2}H$ and d-excess is on the order of a few minutes, the Allan deviation of ^{17}O-excess reaches a minimum (~7 per meg) at an averaging time of about 1 hour (Fig. A1). To assess the precision of calibrated data, a Monte Carlo simulation was applied following Voigt et al. (2022). In 100 000 iterations, random normally distributed values were generated accounting for the standard deviations of (i) raw $\delta^{18}O_V$, $\delta^{2}H_V$ and $^{17}O\text{-excess}_V$, (ii) the coefficients of the mixing ratio dependency functions of each standard (Table A2) and (iii-iv) the measured and reference values of $\delta^{18}O$, $\delta^{2}H$ and ^{17}O-excess of the two standards. In each iteration, raw atmospheric values were calibrated following the above-described procedure.

The Monte Carlo simulation was run for 2-min integration intervals for $\delta^{18}O$, $\delta^{2}H$ and d-excess and for 1-hour integration intervals for ^{17}O-excess. Over 2-min intervals, the raw Allan deviations were 0.11 ‰ for $\delta^{18}O$, 0.65 ‰ for $\delta^{2}H$ and 0.5 ‰ for d-excess, yielding simulated calibrated standard deviations of calibrated 2-min mean values of 0.12 ‰, 1.2 ‰ and 1.6 ‰, respectively. Over 1-hour intervals, the raw Allan deviations were 0.2 ‰ for $\delta^{17}O$, 0.4 ‰ for $\delta^{18}O$, 2.5 ‰ for $\delta^{2}H$, 7 per meg for ^{17}O-excess and 1.6 ‰ for d-excess, yielding simulated standard deviations of calibrated 1-hour mean values of approximately ± 0.2 ‰, ± 0.4 ‰, ± 2.7 ‰ and ± 15 per meg, and ± 4.2 ‰ for $\delta^{17}O$, $\delta^{18}O$, $\delta^{2}H$, ^{17}O-excess, and d-excess, respectively. For consistency, all isotopic tracers were integrated over 1 hour, which also determined the frequency of alternation between measurement heights. This is limited by the resolution achievable for ^{17}O-excess. The simulated standard deviations account for both the measurement precision and the natural variability in the isotopic composition of atmospheric water vapor over the integration interval.

Precipitation was collected in an evaporation-free rainfall collector (Rain Sampler 1, Palmex d.o.o., Zagreb, Croatia; Gröning et al., 2012), sampled monthly from June 2019 to December 2020 and on an event-based interval in 2021. The latter resulted in two snow and 53 rain samples. In addition, an on-site well, an underground spring, two springs in the village Saint-Michel-
160 l'Observatoire and the nearby river Largue were sampled seasonally between May 2020 and October 2021 to constrain the isotopic composition of groundwater. The triple oxygen and hydrogen isotopic composition of precipitation, river, well and spring samples was determined using a second Picarro L2140-i CRDS, operated in ^{17}O-High Precision mode at CEREGE (Aix-en-Provence, France). The measurement protocol was described in detail previously (Vallet-Coulomb et al., 2021). The external reproducibility of a quality control standard (1 SD, n = 10) measured along with the samples in each sequence was
165 ± 0.02‰, ± 0.04‰, ± 0.3‰ and ± 5 per meg, and ± 0.1‰ for $\delta^{17}O$, $\delta^{18}O$, $\delta^{2}H$, ^{17}O-excess, and d-excess, respectively.
To evaluate the significance of monthly variability in the isotopic compositions of precipitation and atmospheric water vapor, we performed pairwise comparisons of monthly values using Student's t-test, and applied a Bonferroni correction (Bland and Altman, 1995). For each pair of months, we compared the average isotopic composition (δ-values) with their standard deviations to determine statistically significant differences.

170 **2.3 Assessment of isotopic (dis)equilibrium between atmospheric water vapor and precipitation**

The isotopic composition of water vapor in isotopic equilibrium with precipitation (hereafter equilibrium water vapor) is estimated from:

$$R_{Veq} = \frac{R_P}{\alpha_{eq,l-v}} \quad (2)$$

where R_{Veq} is the isotopic ratio in water vapor in equilibrium with precipitation, R_P is the measured isotopic ratio in
175 precipitation and $\alpha_{eq,l-v}$ is the liquid-vapor equilibrium isotopic fractionation factor. We used temperature-dependent equilibrium fractionation factors for $^{2}H^{1}HO/^{1}H_2O$ and $^{1}H_2{}^{18}O/^{1}H_2{}^{16}O$ from Majoube (1971). The equilibrium fractionation factor for $^{1}H_2{}^{17}O/^{1}H_2{}^{16}O$ was derived from $^{17}\alpha_{eq,l-v} = {}^{18}\alpha_{eq,l-v}{}^{0.529}$ (Barkan & Luz, 2005). We used T_{air} measured on the ICOS tower at 10 m agl. Note that using T_{air} measured at other heights between 0.4–100 m agl does not significantly influence the results.
180 Like Graf et al. (2019), we denote the differences between equilibrium water vapor and atmospheric water vapor measured at 12.5 m agl as:

$$\Delta\delta^{18}O_{Veq-V} = \delta^{18}O_{Veq} - \delta^{18}O_V \quad (3)$$

$$\Delta d\text{-}excess_{Veq-V} = d\text{-}excess_{Veq} - d\text{-}excess_V \quad (4)$$

$$\Delta^{17}O\text{-}excess_{Veq-V} = {}^{17}O\text{-}excess_{Veq} - {}^{17}O\text{-}excess_V \quad (5)$$

185 A negative value of $\Delta\delta^{18}O_{Veq\text{-}V}$ (Δd-excess$_{Veq\text{-}V}$, Δ^{17}O-excess$_{Veq\text{-}V}$) indicates that $\delta^{18}O$ (d-excess, ^{17}O-excess) of precipitation is lower than expected from isotopic equilibrium with near-surface atmospheric water vapor. Inversely, positive values of $\Delta\delta^{18}O_{Veq\text{-}V}$ (Δd-excess$_{Veq\text{-}V}$, Δ^{17}O-excess$_{Veq\text{-}V}$) indicate that precipitation has higher $\delta^{18}O$ (d-excess, ^{17}O-excess) compared to the expected equilibrium value.

2.4 Weather regimes, air mass back trajectory analysis and oceanic moisture source identification

Synoptic atmospheric variability over Europe can be characterized using weather regimes (Cassou, 2008; Cassou et al., 2005; Michelangeli et al., 1995; Vautard, 1990). Previous studies have demonstrated strong positive correlations between $\delta^{18}O_P$ and $\delta^{2}H_P$ and the NAO index in the temperate and Mediterranean area (Baldini et al., 2008; Field, 2010; Deininger et al., 2016; Zannoni et al., 2019). In addition, Zannoni et al. (2019) reported a negative correlation between both d-excess$_V$ and d-excess$_P$ and the NAO index at a coastal lagoon in Venice. These correlations are strongest in central Europe but are often weaker in mountainous and circum-Mediterranean regions, where local orographic effects and moisture recycling modify the isotopic composition of precipitation (Baldini et al., 2008).

Here, we identify the dominant weather regimes during the study period to assess whether these relationships persist. This may be of interest for paleoclimate reconstructions of NAO circulation patterns based on isotopic records. To this end, large-scale atmospheric circulation fields for the North-Atlantic-European region (20ºN–80ºN and 80ºW–30ºE) were obtained from the European Centre for the Medium-Range Weather Forecasts (ECMWF) ERA5 reanalysis data and classified over 1989–2022. The classification was based on daily-averaged 500 hPa geopotential height (Z500) fields, interpolated onto a 2.5º x 2.5º grid and clustered using the k-means algorithm (Hersbach et al., 2020). Each day was assigned to a specific weather regime based on the criterion of minimum Euclidian distance.

To identify oceanic moisture sources of the local atmospheric water vapor, backward trajectory analysis was performed using the Hybrid Single Particle Lagrangian Integrated Trajectory model (HYSPLIT) (Stein et al., 2015). Meteorological input data were obtained from the Global Data Assimilation System (GDAS) dataset at a spatial resolution of 0.25º x 0.25º. As most of the atmospheric moisture resides in the lowermost 2000 m agl (Bershaw et al., 2012), back-trajectories were initiated at 1500 m agl. Note that back-trajectories initiated at 500 m and 3000 m showed similar paths. Trajectories were computed hourly throughout 2021 extending 168 hours (7 days) backward. This resulted in a total of 8760 trajectories covering 365 measurement days.

Moisture uptake zones were quantified using a Lagrangian moisture source diagnostic following Sodemann et al. (2008). Along each backward trajectory, positive increments in specific humidity ($\Delta q > 0$) calculated at 6-hour intervals were interpreted as moisture uptake from the underlying surface. Each uptake location was assigned to the midpoint of the corresponding trajectory segment. Only uptake events exceeding 0.2 g kg^{-1} and occurring below 1.5 times the planetary boundary layer height were considered in order to reduce the influence of numerical noise and restrict moisture contributions to boundary-layer exchange processes. Each uptake event was weighted by its relative contribution to the final specific humidity at the study site. If a decrease in specific humidity ($\Delta q < 0$), interpreted as precipitation loss, occurred downstream of one or more uptake events, the contributions of the preceding uptakes were proportionally reduced to account for moisture removal. This procedure yields, for each trajectory, the fractional contribution of a grid cell to q at the study site.

In order to assess the potential relation between the isotopic composition of atmospheric water vapor at the study site and its oceanic moisture source region, we applied a modified Concentration Weighted Trajectory (CWT) approach. A spatial grid of

1° × 1° resolution was defined over the study domain. Instead of weighting the isotopic composition measured at the study site by the residence time in each grid cell, as done by Salamalikis et al. (2015), we weighted it by the previously derived fractional moisture contribution $\tau_{(ij)k}$ of the corresponding hourly trajectory. The isotopic signature assigned to each grid cell (i,j) was computed as:

$$C_{ij} = \frac{\sum_{k=1}^{N} \tau_{ijk} C_k}{\sum_{k=1}^{N} \tau_{ijk}} \quad (6)$$

where C_k is the isotopic composition ($\delta^{18}O$, d-excess, or ^{17}O-excess) measured upon arrival of trajectory k at the study site, and τ_{ijk} is the fractional moisture contribution of grid cell (i,j) to trajectory k. Thus, C_{ij} represents the moisture-contribution-weighted isotopic composition associated with evaporation from grid cell (i,j). For precipitation, all air mass back-trajectories of hours during which rain was detected on-site were compiled and weighted by rainfall amount.

For regional interpretation, we aggregated grid cells into eight predefined source regions after Sodemann and Zuber (2010): NW = Northwest North Atlantic, NE = Northeast North Atlantic, SW = Southwest North Atlantic, SE = Southeast North Atlantic, A = Arctic and Nordic Seas, CE = Central Europe, MW = Western Mediterranean, ME = Eastern Mediterranean. To focus on oceanic moisture sources, only grid cells located over ocean surfaces were considered. Continental areas were masked using the GLDAS Land/Sea Mask Dataset at 1º resolution (NASA/GES DISC., 2026).

2.5 Climate conditions and isotopic composition of the atmospheric water vapor at the oceanic moisture sources

Monthly averages of sea surface temperature (SST), T_{air} and dew point temperature at 2 m above the ocean surface (T_{dew}) were obtained from ERA5 hourly data for the region spanning 20º-70ºN latitude and -50º-40ºE longitude (Hersbach et al., 2020). RH over the ocean was derived from T_{air} and T_{dew} and subsequently normalized to SST (RH_{SST}).

The triple oxygen and hydrogen isotopic composition of water vapor evaporated from the ocean was estimated using a simple evaporation model (Craig & Gordon, 1965), assuming that all water vapor above the ocean is derived from local evaporation (i.e. the closure assumption; Merlivat & Jouzel, 1979). Seawater $\delta^{18}O$ and d-excess values were taken from the CISE-LOCEAN seawater isotopic database (waterisotopes-CISE-LOCEAN, 2014) and range from 0.3 to 1.3‰ and -0.9 to -2.3‰, respectively. For ^{17}O-excess of seawater, the global average value of -5 per meg from the only existing compilation is used (Luz & Barkan, 2010). The turbulence coefficient is an empirical parameter that quantifies the contribution of molecular diffusion to the total kinetic fractionation during evaporation. Several studies have attempted to constrain this parameter empirically (e.g., Pfahl and Wernli, 2008; Uemura et al., 2010; Zannoni et al., 2022) and to develop theoretical frameworks (Horita et al., 2008; Xia et al. 2023; Duetsch et al., 2025). The turbulence coefficient has been adjusted to 0.33, which is at the upper end of previously reported values for open-ocean evaporation (see, e.g., Gat, 1996; Pfahl & Wernli, 2008; Uemura et al., 2010, Duetsch et al., 2025). Lower turbulence coefficients correspond to lower kinetic fractionation during evaporation and therefore lower d-excess and ^{17}O-excess values in the evaporated water vapor.

3 Results

3.1 Variability of local meteorological parameters, phenology, stomatal conductance and transpiration

In 2021, annual average T_{air} and RH at O_3HP were 12 ºC and 63 %, respectively. The annual precipitation was 730 mm, which is about 150 mm lower than the average annual precipitation from 2008-2020 (Reiter et al., 2015). As typical for a Mediterranean climate, more than 70 % of precipitation occurred from April to May and from September to December, while summer months were the driest (Fig. 2a). The monthly atmospheric water mixing ratio (χ) ranged from 7 mmol mol^{-1} in winter to 22 mmol mol^{-1} in summer. Despite the increase in χ during summer, the lowest monthly average RH was recorded in August (53 %), while the highest was observed in February (75 %), due to higher monthly average T_{air} in summer (JJA, 21ºC) than in winter (DJF; 6ºC). The daily average maximum planetary boundary layer height increased from 600 m agl in December to 1700 m agl in July. The average wind speed at 10 m height over daily mean values was 2.6 ± 1.1 m s^{-1} in 2021. One to eight windy days (daily average wind speed > 4 m s^{-1}; Obermann et al., 2018) were observed per month. Windy days are mostly indicative for Mistral conditions – a strong northerly wind typical of the Provence region – and occurred most frequently in winter and spring.

In 2021, daytime average χ was 2 to 6 mmol mol^{-1} higher than at night. Daytime average T_{air} was 6 to 16ºC higher than at night, while average RH increased by 26 to 50 % from day to night. The largest day-night differences occurred near the ground and in summer (Fig. B1-B3). During the day, χ and T_{air} were highest near the ground, whereas RH was vertically homogenous (Fig. B1-B3). At night, the vertical gradient in T_{air} and χ weakened. Nighttime cooling resulted in higher RH that decreased from the surface to 10 m agl (Fig. B1-B3).

The first oak buds appeared in mid-April 2021. The oak leaves matured in May and senesced in November. Their stomatal conductance and transpiration followed the diurnal cycle of global solar radiation and RH (Fig. B4). During the three separate days of continuous measurement, daytime stomatal conductance and transpiration ranged from 20–60 mmol mol^{-1} and 0.5–1.8 mmol mol^{-1}, respectively. During the night, transpiration and stomatal conductance were always lower than 20 mmol mol^{-1} and 0.1 mmol mol^{-1}, respectively. Transpiration was highest at the beginning of the growing season in June, and the lowest in August, mainly due to lower stomatal conductance in oaks cope with the water stress (high vapor pressure deficit).

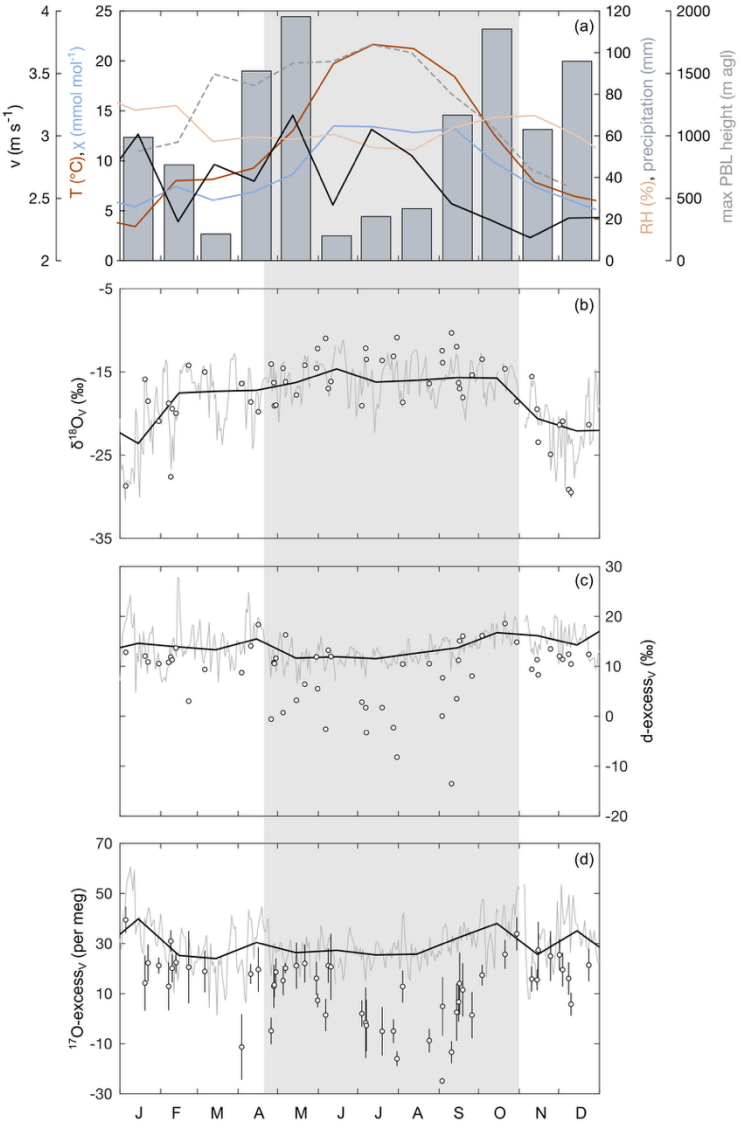

Figure 2: Time series of meteorological data and the isotopic composition of atmospheric water vapor measured at 12.5 m agl and estimated from isotopic equilibrium with precipitation in 2021. (a) Monthly precipitation amount and monthly average temperature (T_{air}), atmospheric water mixing ratio (χ), wind speed (v), and relative humidity (RH) measured at 10 m agl. The grey dashed line shows the monthly average maximum planetary boundary layer height for the 0.25°×0.25° grid field covering the study site (Guo et al., 2022). (b)-(d) Solid lines represent daily (grey) and monthly (black) average isotopic composition of atmospheric water vapor measured at 12.5 m agl. Circles show the isotopic composition of water vapor estimated from isotopic equilibrium with event-based precipitation samples using T_{air} observed at 10 m agl. Note that the error bars for $\delta^{18}O$ and d-excess are smaller than symbol size. The grey shaded area marks the oak forest growing season.

3.2 Isotopic composition of precipitation and groundwater

The annual amount-weighted average isotopic values of precipitation in 2021 were -7.5 ± 2.3 ‰ for $\delta^{18}O_P$, -48.1 ± 20.2 ‰ for $\delta^{2}H_P$, 11.6 ± 3.5 ‰ for d-excess$_P$ and 27 ± 9 per meg for ^{17}O-excess$_P$ (Fig. 3). These values are close to those obtained for 2020

and indistinguishable from those obtained for the whole precipitation dataset from June 2019 to December 2021 (Table B1). The springs, the well and the river Largue sampled seasonally between December 2020 and October 2021 showed little spatial and seasonal isotopic variability (Table B1) and averaged to -7.3 ± 0.5 ‰ for $\delta^{18}O$, -47.0 ± 3.6 ‰ for $\delta^{2}H$, 11.2 ± 0.6 ‰ for d-excess and 29 ± 5 per meg for ^{17}O-excess. These values coincide with the annual amount-weighted average isotopic composition of precipitation.

Monthly amount-weighted average isotopic values of precipitation varied between -11.8 ‰ and -1.1 ‰ for $\delta^{18}O_P$, between -78.8 ‰ and -6.5 ‰ for $\delta^{2}H_P$, between -1.4 ‰ and 18.2 ‰ for d-excess$_P$ and between 1 per meg and 41 per meg for ^{17}O-excess$_P$ (Table B1). In general, monthly values of $\delta^{18}O_P$ and $\delta^{2}H_P$ were low in winter and varied in their upper range from spring to autumn. Inversely, monthly values of d-excess$_P$ and ^{17}O-excess$_P$ were low in summer and tended to higher values in autumn and winter.

The isotopic values of event-based rain samples ranged from -18.4 ‰ to -0.2 ‰ for $\delta^{18}O_P$, from -142.5 ‰ to -7.8 ‰ for $\delta^{2}H_P$, from -13.0 ‰ to 20.5 ‰ for d-excess$_P$ and from -15 per meg to 51 per meg for ^{17}O-excess$_P$ (Table B1). The two snow samples had the lowest $\delta^{18}O_P$ (-22.3 ‰ and -18.4 ‰, respectively) and $\delta^{2}H_P$ (-162.9 ‰ and -142.5‰, respectively) of the whole data set, while d-excess$_P$ (15.6 ‰ and 4.0 ‰) and ^{17}O-excess$_P$ (68 per meg and 17 per meg) were variable. The seasonal variability of ^{17}O-excess$_P$ was generally higher than its variability from one event to another. In contrast, variability of $\delta^{18}O_P$ and d-excess$_P$ was often higher on event-scale than on seasonal scale (Student's t-test).

Linear regression through monthly amount-weighted average precipitation data for 2020 and 2021 (n = 22) gives (Fig. 3):

$$\delta^{2}H = 7.9\ (\pm 0.4)\ \delta^{18}O + 9.7\ (\pm 2.7) \quad (7)$$

$$\delta'^{17}O = 0.5263\ (\pm 0.0009)\ \delta'^{18}O + 0.0128\ (\pm 0.0064) \quad (8)$$

In the $\delta^{2}H$-$\delta^{18}O$ system, the slope of the regression line is indistinguishable from that for Avignon GNIP station (IAEA/WMO, 2024), located 70 km to the west of our study site (Fig. 3). It is close to that of the GMWL (8; Rozanski et al., 1993), but higher than the range of previously reported values for the western Mediterranean area (7.15-7.56; Celle-Jeanton et al., 2001; Giménez et al., 2021; Saighi, 2005). In the $\delta'^{17}O$-$\delta'^{18}O$ system, the slope of the regression line is lower than that of the GMWL (0.528; Luz & Barkan, 2010; Terzer-Wassmuth et al., 2023) but similar to the value obtained for temperate and intertropical areas (0.5265; Sharp et al., 2018; Terzer-Wassmuth et al., 2023). Notably, the slope of the regression line varies strongly from 2020 to 2021 for both the $\delta^{2}H$-$\delta^{18}O$ system (7.3-8.5) and the $\delta'^{17}O$-$\delta'^{18}O$ system (0.5254-0.5271). A longer precipitation isotopic record is required to establish a robust local meteoric water line for the study site.

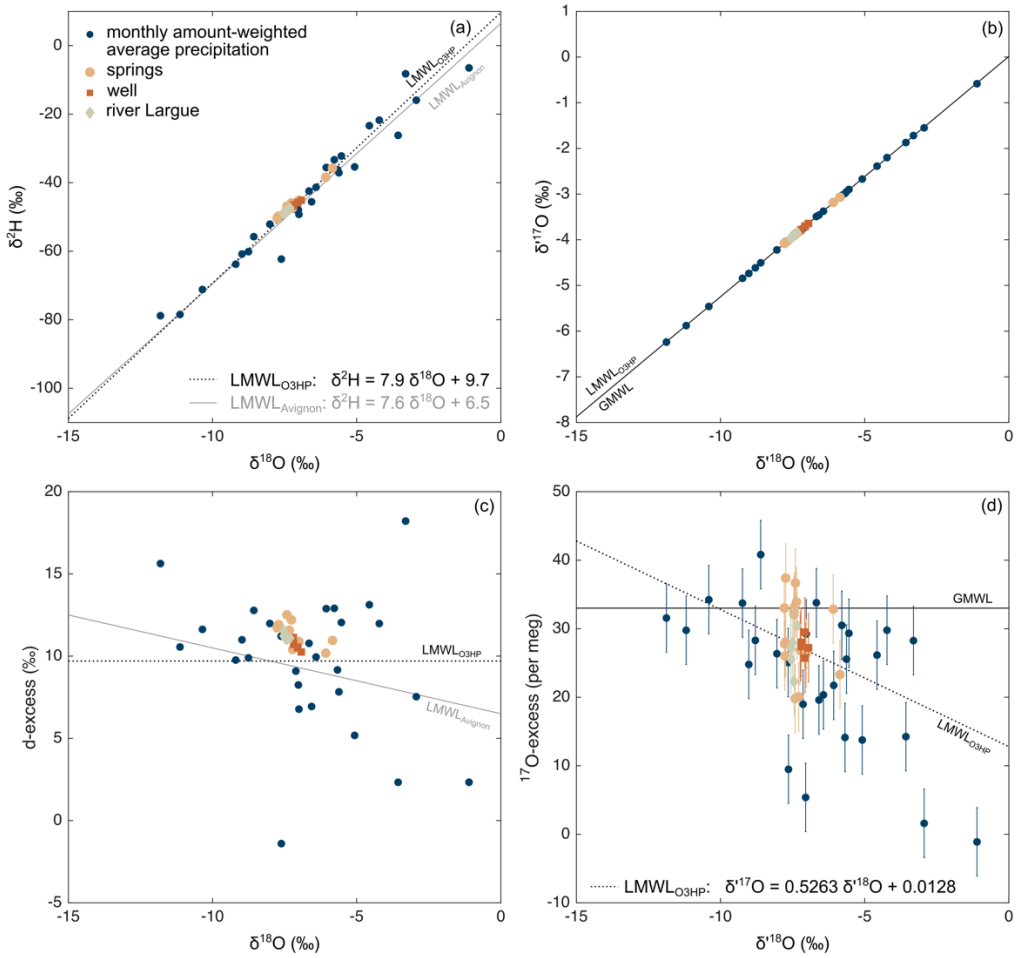

Figure 3: (a) δ^2H vs $\delta^{18}O$, (b) $\delta'^{17}O$ vs $\delta'^{18}O$, (c) d-excess vs $\delta^{18}O$ and (d) ^{17}O-excess vs $\delta'^{18}O$ of local meteoric waters collected in this study. Blue circles represent the monthly amount-weighted average isotopic composition of precipitation collected at O_3HP between June 2019 and December 2021. Pale orange circles, orange squares and grey diamonds show the isotopic composition of samples taken from springs, a well and the nearby river *Largue* in the surroundings of the study site (Table B1). The linear regression line through precipitation isotopic data from 2020 and 2021 is indicated by the black dotted line. In addition, (a) and (c) show the local meteoric water line (LMWL) of Avignon for comparison (data derived from the global network of isotopes in precipitation (GNIP) database; IAEA/WMO, 2024). No ^{17}O-excess data was available for the Avignon dataset. Therefore, (b) and (d) show the global meteoric water line (GMWL) for comparison. Note that error bars of $\delta^{17}O$, $\delta^{18}O$, δ^2H and d-excess are smaller than symbol size.

3.3 Isotopic composition of atmospheric water vapor

The annual average isotopic composition of atmospheric water vapor at 12.5 m agl was -17.7 ± 2.8 ‰ for $\delta^{18}O_V$, -128.1 ± 21.9 ‰ for δ^2H_V, 13.8 ± 1.7 ‰ for d-excess$_V$ and 30 ± 5 per meg for ^{17}O-excess$_V$, and indistinguishable from that measured at lower heights. Similar to precipitation, $\delta^{18}O_V$ and δ^2H_V were low in winter (-23.6 ‰ and -174.2 ‰, respectively) and high from spring to autumn, peaking in June (-14.6 ‰ and -105.2 ‰, respectively) (Table B2). Values of d-excess$_V$ were high in October and November (> 16 ‰) and low from May to July (< 12 ‰). In contrast, ^{17}O-excess$_V$ varied little throughout the

year (from 24 per meg to 40 per meg). Low values (25-27 per meg) were recorded between May and August 2021, while highest values were observed in December (35 per meg) and January (40 per meg).

Day-to-day isotopic variability of atmospheric water vapor was high (up to 9.3 ‰, 16.0 ‰ and 27 per meg for $\delta^{18}O_v$, d-excess$_v$ and ^{17}O-excess$_v$, respectively) and exceeded monthly and seasonal variability for d-excess$_v$ and ^{17}O-excess$_v$ (Fig. 2). There is no statistically significant difference in the daily average isotopic composition of atmospheric water vapor on rainy and non-rainy days, indicating that precipitation had no significant influence on the isotopic composition of near-surface atmospheric water vapor on daily and monthly scale.

Diurnal patterns of d-excess$_v$ and ^{17}O-excess$_v$ changed from a season to another (Fig. B6-B7). They can be illustrated by two examples (Fig. 4): In June, the month with the most active leaf gas exchange in the Mediterranean (Bartsch et al., 2020), d-excess$_v$ and ^{17}O-excess$_v$ were lowest at sunset and highest at noon, coinciding at noon with minimum RH, maximum transpiration and maximum χ measured under the forest canopy. In December, a month characterized by the absence of alive tree foliage and transpiration and a thin planetary boundary layer, the amplitude of the diurnal cycle was three times lower than in June for the d-excess$_v$ and more than 15 times lower for the ^{17}O-excess$_v$. Diurnal isotopic patterns were consistent for different heights, but the magnitude of variations decreased with distance from ground. Vertical isotopic gradients were generally stronger during night, in line with limited atmospheric turbulent convection (Fig. B5).

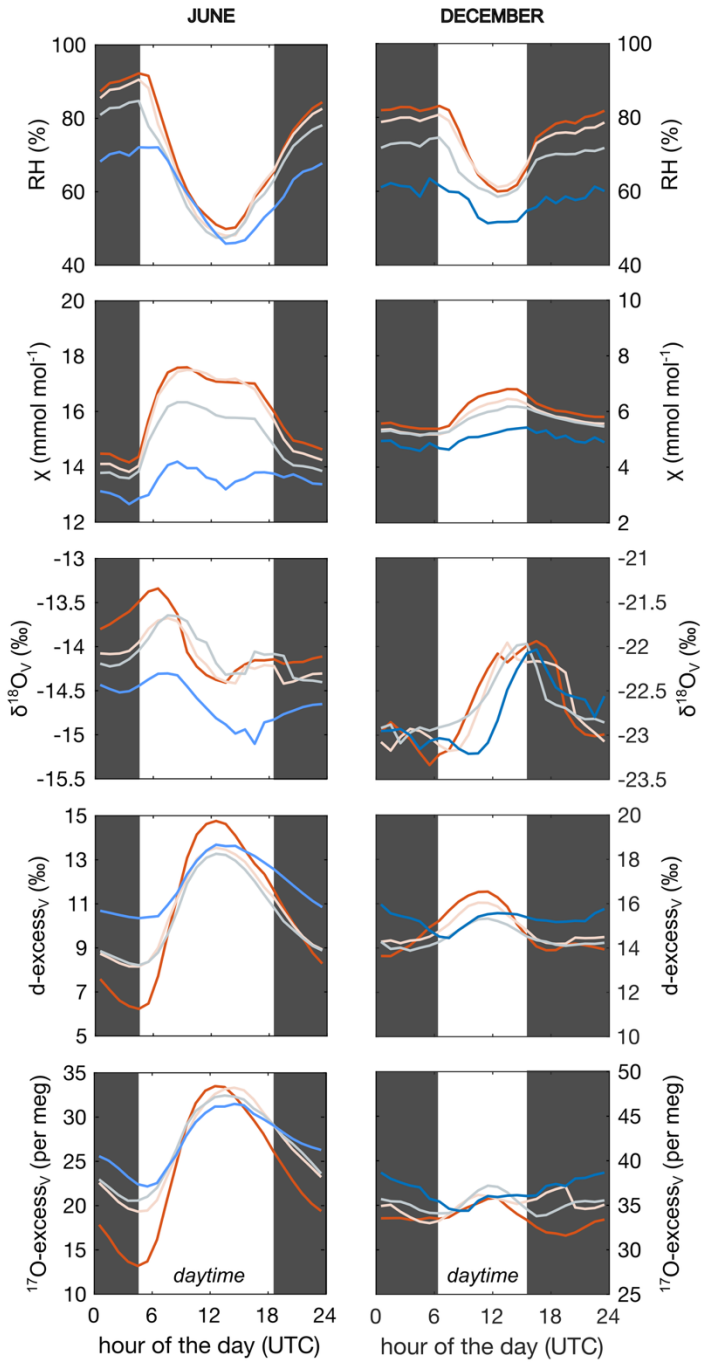

Figure 4: Monthly average daily cycle of relative humidity (RH), atmospheric water mixing ratio (χ) and $\delta^{18}O_V$, d-excess$_V$ and ^{17}O-excess$_V$ of atmospheric water vapor at different measurements heights: above the grass plot (0.4 m agl; red), and below (1.5 m agl; pale), within (3.5 m agl; grey) and above (12.5 m agl, blue) the oak forest canopy. The left panels show monthly averages for June 2021, while the right panels show monthly averages for December 2021. For December, only the period from 01 to 25 December is included due to the lack of isotopic data at 0.4 m, 1.5 m and 3.5 m after this date. Grey shaded areas represent night-time periods. Note that the vertical axes for June and December use similar scales but with different offsets.

3.4 Isotopic (dis)equilibrium between precipitation and near-surface atmospheric water vapor

In winter, spring and late autumn, $\delta^{18}O_{Veq}$ was up to 5.5 ‰ lower than $\delta^{18}O_V$, while in summer $\delta^{18}O_{Veq}$ was up to 3.7 ‰ higher than $\delta^{18}O_V$. Values of d-excess$_{Veq}$ were generally close to d-excess$_V$ in winter, but up to 16 ‰ lower than d-excess$_V$ during the oak growing season. Values of ^{17}O-excess$_{Veq}$ were slightly lower than ^{17}O-excess$_V$ in winter (~15 per meg) and up to 44 per meg lower during the oak growing season (Fig. 5).

However, on annual scale, $\delta^{18}O_V$ (-17.8 ± 2.8 ‰), $\delta^{2}H_V$ (-128.3 ± 21.9 ‰) and d-excess$_V$ (13.8 ± 1.7 ‰) were similar to their values expected from isotopic equilibrium with precipitation (-17.8 ± 2.7 ‰, -130.1 ± 21.6 ‰ and 12.3 ± 3.1‰, respectively). In contrast, ^{17}O-excess$_V$ (30 ± 5 per meg) was in annual average 14 per meg higher than ^{17}O-excess$_{Veq}$ (16 ± 10 per meg).

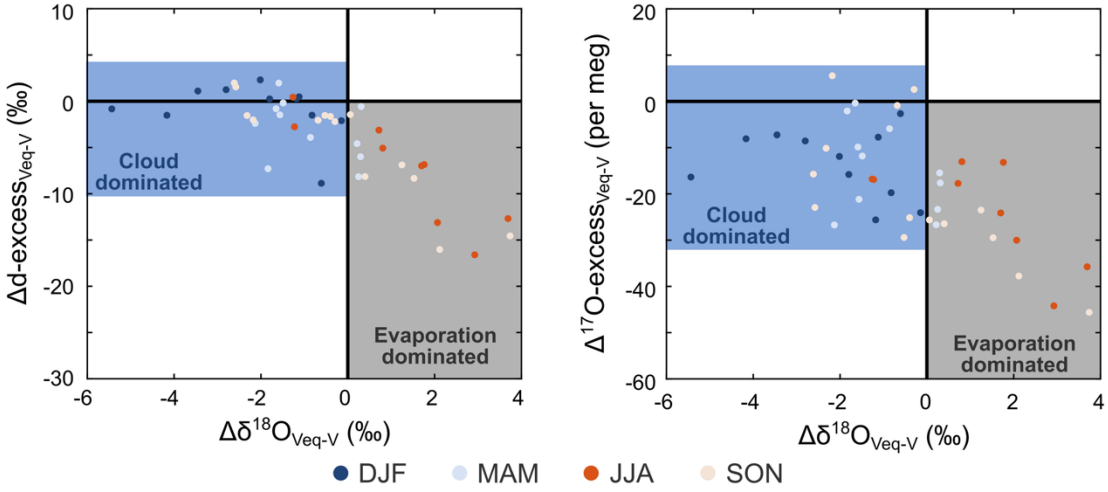

Figure 5: Isotopic difference (Δ) between water vapor estimated from isotopic equilibrium with precipitation (V_{eq}) and amount-weighted atmospheric water vapor measured at 12.5 m above ground level (V) for each precipitation event in 2021. Data is coloured according to season. The blue-shaded area indicates samples for which the equilibration between precipitation and near-surface atmospheric water vapor is likely incomplete. Precipitation samples that correspond to data falling within the grey-shaded area are likely affected by re-evaporation during fall through the air column.

3.5 Relationships between meteorological parameters, phenology, stomatal conductance, transpiration and the isotopic compositions of atmospheric water vapor and precipitation

Monthly average $\delta^{18}O_V$ was strongly correlated with T_{air} and χ (r^2 = 0.67 and 0.63, respectively). In contrast, d-excess$_V$ was only weakly correlated with these variables (r^2 = 0.26 and 0.29, respectively), and ^{17}O-excess$_V$ showed no significant relationship (Fig. B8). There was no correlation between the monthly average isotopic composition of atmospheric water vapor and RH or wind speed.

Hourly means of $\delta^{18}O_V$, d-excess$_V$ and ^{17}O-excess$_V$ averaged by month (Fig. B6-B7) were strongly correlated with RH, T_{air} and transpiration during the oak forest growing season (r^2 > 0.55, > 0.73 and > 0.64, respectively). Correlations between ^{17}O-excess$_V$ and d-excess$_V$ were also strong during the oak forest growing season (r^2 = 0.52–0.93), peaking in June, whereas they were not correlated in winter.

For precipitation, monthly average $\delta^{18}O_P$ and d-excess$_P$ were weakly correlated with χ, T_{air} and RH ($0.28 \leq r^2 \leq 0.38$), whereas ^{17}O-excess$_P$ showed stronger correlations with these variables ($0.44 \leq r^2 \leq 0.61$). No correlation was observed between the monthly average isotopic composition of precipitation and precipitation amount.

At the event scale, $\delta^{18}O_P$ and ^{17}O-excess$_P$ remained weakly correlated with T_{air} ($r^2 = 0.41$ and 0.43, respectively) and χ ($r^2 = 0.34$ and 0.29, respectively), while d-excess$_P$ showed little or no correlation ($r^2 < 0.23$) (Fig. B9). Event-based isotopic values of precipitation showed no correlation with RH or precipitation amount.

3.6 Relationships between moisture sources and the isotopic composition of atmospheric water vapor and precipitation

The moisture source contributions for atmospheric water vapor and precipitation are illustrated in Figure C1 and C2. For atmospheric water vapor, the NE North Atlantic (33%) and the Western Mediterranean (29%) are the dominated moisture sources for our study site (Table C1). For precipitation, most of the moisture is derived from the Western Mediterranean (41%), followed by the NE North Atlantic (25%) and the SE North Atlantic (18%) (Table C2). Changes in the relative contributions of each moisture source over the year are illustrated in Figure C3 and C4 for atmospheric water vapor and precipitation, respectively.

The isotopic compositions of atmospheric water vapor and precipitation clustered by moisture sources were generally similar (Table C1 and C2). In particular, d-excess and ^{17}O-excess of atmospheric water vapor or precipitation coming from the North Atlantic sectors and the Western Mediterranean were not significantly different.

We also compared the monthly average isotopic composition of atmospheric water vapor observed at O_3HP with those estimated above the four oceanic moisture sources (Fig. 6). The latter shows seasonal isotopic variability which co-varies with SST and RH_{SST}. Interestingly, from July to December, RH_{SST} over the Mediterranean Sea is systematically lower than over the NE North Atlantic but does not differ from RH_{SST} over the SE North Atlantic. For all sources, $\delta^{18}O_V$ is higher and d-excess$_V$ and ^{17}O-excess$_V$ are lower in summer than in winter. A similar seasonal trend is evident in the isotopic composition of the water vapor observed at O_3HP (Fig. 6). However, the $\delta^{18}O_V$ values at O_3HP were 3–11 ‰ lower than those estimated for the ocean sources. In contrast, the d-excess$_V$ at O_3HP was of the same order of magnitude as that over the ocean sources, while the observed ^{17}O-excess$_V$ was slightly higher (by 11 ± 5 per meg).

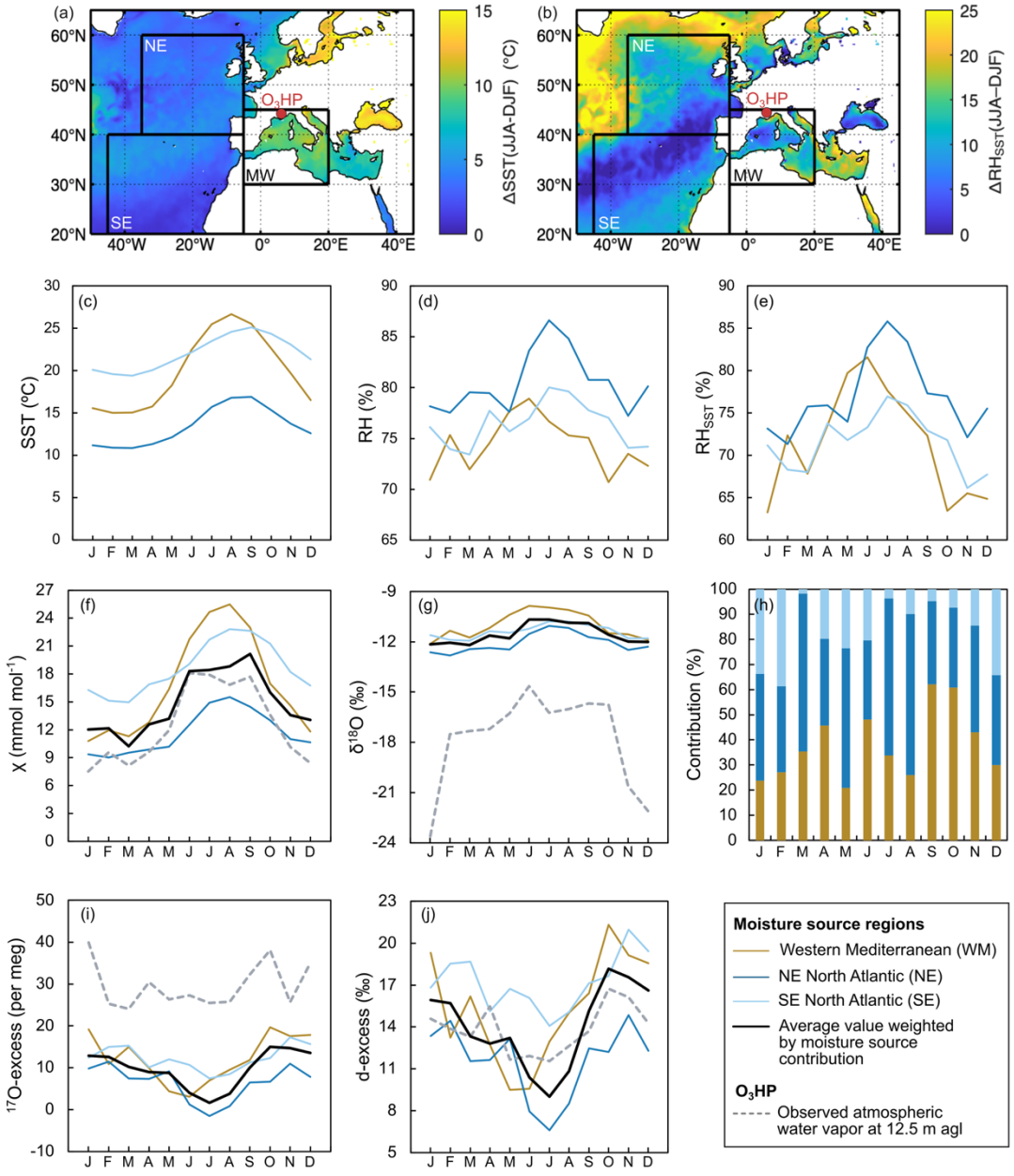

Figure 6: Seasonal and monthly variation in the isotopic composition of atmospheric water vapor measured at O_3HP compared with climate parameters and isotopic composition of atmospheric water vapor at the three main oceanic moisture sources. (a)-(b) Spatial variability of the difference between summer (JJA) and winter (DJF) sea surface temperature (SST) and relative humidity normalized to SST (RH_{SST}) in 2021. Data derived from ERA5 Reanalysis (Hersbach et al., 2020). The red circle indicates the location of the study site. (c)-(e) Monthly average SST, relative humidity above the ocean (RH) and RH_{SST} obtained from the ERA5 reanalysis dataset (Hersbach et al., 2020) for 2021. (f)-(j) Monthly average of atmospheric water mixing ratio (χ), relative contribution of the three moisture sources obtained from Lagrangian moisture source diagnostic (Sect. 3.6), $\delta^{18}O_V$, d-$excess_V$ and ^{17}O-$excess_V$ measured at O_3HP at 12.5 m agl (dashed line) and estimated above the three main oceanic moisture sources (solid lines). See Sect. 2.5 for more details on how the isotopic composition of water vapor over each moisture source is estimated.

3.7 Relationship between weather regimes and the isotopic compositions of atmospheric water vapor and precipitation

Four weather regimes were identified for wintertime (November–March) 2021 in the North Atlantic area: the negative North Atlantic Oscillation (NAO^-), the positive North Atlantic Oscillation (NAO^+), the Scandinavian Blocking regime, and the Atlantic Ridge regime (Fig. C5). The Atlantic Ridge and NAO^- regimes were dominant, whereas NAO^+ occurred only sporadically. In summer 2021 (May–September), the NAO^-, Icelandic Low, Atlantic Low, and Scandinavian Blocking/NAO+ regimes were identified. The Blocking/NAO+ regime was clearly the dominant, followed by NAO^-. Precipitation occurred most frequent during NAO^- phases (Fig. C6c, d). The isotopic compositions of water vapor and precipitation grouped by weather regime did not show significant differences (Fig. C6).

4 Discussion

The isotopic compositions of atmospheric water vapor and precipitation are determined by the evaporative conditions at the oceanic moisture sources, eventually modified by processes occurring during atmospheric transport and precipitation formation. These processes include progressive rainout, mixing of air masses from different sources, and the regional or local recycling of moisture through evapotranspiration from soil, plant and open surface waters. Locally, equilibration of raindrops with surrounding atmospheric water vapor and sub-cloud re-evaporation during falling can modify the isotopic composition of precipitation. In convective storms, vertical diffusion and mixing can additionally occur. The isotopic effects of these processes are physically well understood and have been modelled with differing degrees of complexity (Risi et al., 2012; Tremoy et al., 2014; Galewsky et al., 2016 and references therein; Xia et al., 2022, 2023). They are summarized in Figure 7. However, little is known about the combined effects of these factors on the triple oxygen isotopic composition in atmospheric water vapor and precipitation, as long-term records are still scarce for precipitation and non-existent for water vapor. Our long-term monitoring of the triple oxygen and hydrogen isotopic composition of atmospheric water vapor and precipitation at the O_3HP site allows us to assess the combined effect of these processes across different time scales. Further, the isotopic differences observed between the measured atmospheric water vapor and that estimated from isotopic equilibrium with precipitation are discussed.

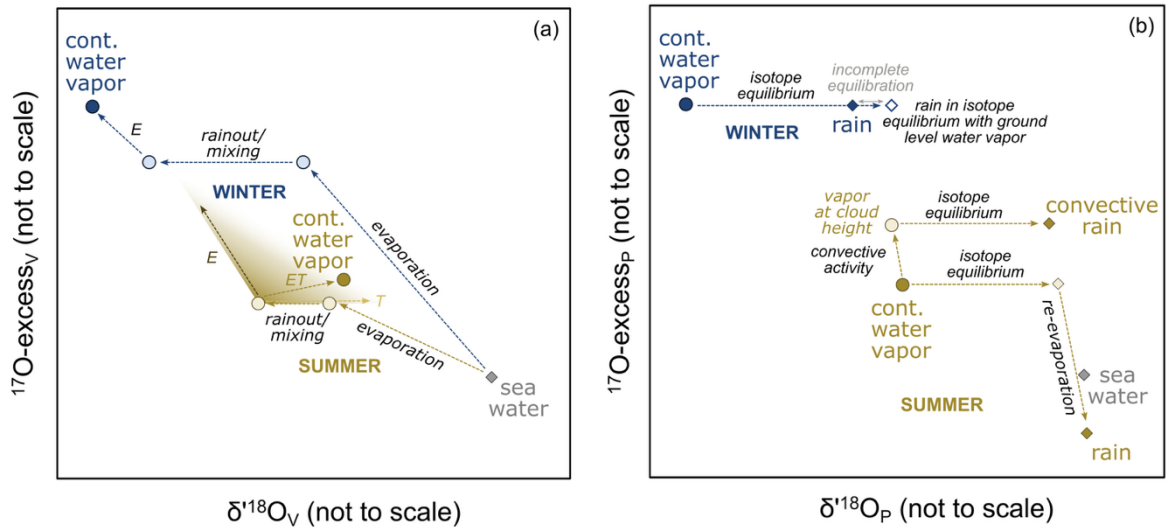

Figure 7: Synthesis of the effect of ocean evaporation, rainout, air mass mixing, continental moisture recycling (ET) resulting from evaporation (E) and plant transpiration (T), and post formation precipitation processes in winter (blue) and summer (yellow) on the triple oxygen isotopic composition of (a) atmospheric water vapor and (b) precipitation (see Sect. 4 for further details).

4.1 Evaporative conditions at the oceanic moisture sources

The three principle oceanic moisture sources show lower RH_{SST} during winter than in summer, resulting in stronger kinetic fractionation during evaporation from the ocean and higher d-excess$_V$ and ^{17}O-excess$_V$ in the evaporated water vapor in winter than in summer (Fig. 6). This seasonal change predicted for water vapor over the oceanic moisture sources is also visible in the d-excess$_V$ measured at O_3HP and to a lesser extent in the ^{17}O-excess$_V$. This consistency suggests that seasonal changes in evaporative conditions at the oceanic moisture sources contribute to seasonal changes in d-excess$_V$ and ^{17}O-excess$_V$ at the study site. This is in agreement with previous interpretations of the triple oxygen isotopic composition of water vapor and precipitation (Affolter et al., 2015; Landais et al., 2012; Liotta et al., 2008; Merlivat & Jouzel, 1979; Pfahl & Sodemann, 2014; Tian et al., 2018; Uechi & Uemura, 2019). However, with regard to $\delta^{18}O_V$, seasonal changes in the evaporative conditions at the oceanic moisture sources are limited to 1.5 ‰ and cannot explain the ~7 ‰ seasonal variations observed at the study site. This indicates that $\delta^{18}O_V$ is likely modified by further fractionation processes.

In previous studies, evaporative conditions at the moisture sources were invoked to explain d-excess$_P$ in precipitation from the Western Mediterranean (~14 ‰) to be higher than in precipitation from the NE North Atlantic (~10 ‰) (Casellas et al., 2019; Celle-Jeanton et al., 2001; Cruz-San Julian et al., 1992; Delattre et al., 2015; Natali et al., 2021). Theoretical predictions indeed show that d-excess$_V$ over NE North Atlantic is about 3.7 ‰ lower than over Western Mediterranean due to higher RH_{SST} (Fig. 6). Similarly, ^{17}O-excess of water vapor evaporated from the Western Mediterranean is predicted to be ~ 6 per meg higher than from the NE North Atlantic, although the magnitude remains within measurement precision. However, d-excess and ^{17}O-excess measured in atmospheric water vapor and precipitation at O_3HP grouped by their primary moisture source (NE North Atlantic vs. Mediterranean) were not significantly different. Several factors may have contributed to diminish the isotopic

contrast between these source regions, including frequent mixing of moisture from multiple sources, local orographic and boundary-layer dynamics or moisture recycling during atmospheric transport (Aemisegger et al., 2014; Natali et al., 2022).

4.2 Rayleigh distillation during air mass transport

Along the air mass trajectory, the water vapor undergoes Rayleigh distillation due to the progressive rainout. Rainout is forced by a decrease in temperature, accompanied by a decrease of χ and leads to a decrease of $\delta^{17}O_V$, $\delta^{18}O_V$ and $\delta^{2}H_V$ and subsequent precipitation (Dansgaard, 1964; Galewsky et al., 2016). Rayleigh distillation explains why the monthly average $\delta^{18}O_v$ is systematically lower than at the oceanic moisture sources (Fig. 6). Furthermore, enhanced rainout along the longer transport distance from the North Atlantics likely explain why the $\delta^{18}O_V$ derived from the NE North Atlantic is 1 to 3 ‰ lower than $\delta^{18}O_V$ from the Western Mediterranean (Delattre et al., 2015; Natali et al., 2021).

In contrast, Rayleigh distillation has limited impact on d-excess$_V$ and ^{17}O-excess$_V$ as, by definition, these parameters are weakly sensitive to equilibrium isotopic fractionation (Merlivat & Jouzel, 1979; Xia et al., 2023). In mid-latitudes Rayleigh distillation is expected to cause up to 3 ‰ changes in d-excess$_V$, with the direction of change depending on the season and the degree of distillation (Xia et al., 2022). The effect should not exceed a 5 per meg increase for ^{17}O-excess$_V$ (Xia et al., 2023). Nevertheless, enhanced rainout along transport pathways from the North Atlantic may have attenuated potential moisture source differences in d-excess$_V$ and ^{17}O-excess$_V$.

4.3 Terrestrial moisture recycling

On a daily scale, χ, d-excess$_V$ and ^{17}O-excess$_V$ are higher and $\delta^{18}O_V$ is lower during the day (with a peak in the afternoon) than at night. Such a day-night pattern has been reported for d-excess$_V$ across diverse environments, including forests, grasslands, wetlands, agricultural areas and urban regions (Berkelhammer et al., 2013; Delattre et al., 2015; Welp et al., 2012) and attributed to several processes, including entrainment of the residual layer or air from the lower free troposphere in the boundary layer (Lai & Ehleringer, 2011; Simonin et al., 2014), local evapotranspiration fluxes (Huang & Wen, 2014; Simonin et al., 2014; Welp et al., 2012; Zhao et al., 2014; Delattre et al., 2015), and dewfall evaporation (Bastrikov et al., 2014; Berkelhammer et al., 2013). The fact that the observed day-night pattern in d-excess$_V$ and ^{17}O-excess$_V$ is more pronounced during the forest growth period and most pronounced near surface (Fig. 4) supports the key influence of surface-atmosphere processes. Assuming that the soil water has an isotopic composition close to that of precipitation, soil water evaporation decreases $\delta^{18}O_V$ and increases d-excess$_V$ and ^{17}O-excess during the day (Craig & Gordon, 1965; Rothfuss et al., 2021; Fig. 7). Plant transpiration, which is assumed to be non-fractionating relative to soil water (Galewsky et al., 2016 and references therein) increases $\delta^{18}O_V$ but has little impact on d-excess$_V$ and ^{17}O-excess$_V$ (Fig. 7). In total, net evapotranspiration affects $\delta^{18}O_V$, with the direction and magnitude depending on the relative contributions of evaporation and transpiration, whereas d-excess$_V$ and ^{17}O-excess$_V$ are elevated only when evaporation is substantial (Fig. 7). Entrainment of a remnant of the convective boundary layer of the previous day, with a high d-excess$_V$ and ^{17}O-excess$_V$ used by evapotranspiration, may amplify the

increase in d-excess$_V$ and ^{17}O-excess$_V$ in the morning (Lai & Ehleringer, 2011; Simonin et al., 2014,Griffis et al. 2016; Welp et al., 2012). Entrainment of the lower free troposphere may also occur. However, the low water vapor mixing ratio of the free troposphere (< 4000 ppmv) likely limits its influence on the isotopic composition of atmospheric water vapor. During the night, when RH is high, water exchange between plant water subjected to incomplete stomata closure, or evaporated surface soil waters, and the atmospheric water vapor can increase $\delta^{18}O_V$ and decrease d-excess$_V$ (Berkelhammer et al., 2013; Bastrikov et al., 2014; Lai & Ehleringer, 2011; Simonin et al., 2014; Welp et al., 2012) and ^{17}O-excess$_V$. The combination of all these factors likely contributes to the observed day-night pattern in $\delta^{18}O_V$, d-excess$_V$ and ^{17}O-excess$_V$. On the monthly scale, these day-night vegetation-related isotopic variations cancel each other out. This contradicts the previously proposed hypothesis that continental evaporation masks the correlation between NAO and $\delta^{18}O_P$ in the circum-Mediterranean area (Baldini et al. 2008).

4.4 Mixing between air masses

The mixing of air masses from different origins frequently occurs during atmospheric transport. The mixing of two air masses with different $\delta^{18}O_V$ but similar ^{17}O-excess$_V$ and d-excess$_V$ results in a decrease in ^{17}O-excess$_V$, while d-excess$_V$ remains largely unchanged. The effect on ^{17}O-excess$_V$ differs from that on d-excess$_V$ due to its logarithmic (non-linear) δ' notation (Li et al., 2015; Aron et al., 2021; Leuenberger and Ranjan, 2021). The decrease in ^{17}O-excess$_V$ due to mixing is however small, representing only 3 per meg for a $\delta^{18}O_V$ difference of 10 ‰ between two air masses with the same water content (Xia et al., 2023). As isotopic differences in atmospheric water vapor observed between the oceanic moisture sources are small, mixing of air masses from different oceanic sources is unlikely to significantly alter the isotopic composition of atmospheric water vapor observed at the O_3HP site.

4.5 Precipitation formation, raindrop re-evaporation, and isotopic (dis)equilibrium with atmospheric water vapor

Liquid precipitation forms in isotopic equilibrium with atmospheric water vapor at cloud height, while ice formation may be accompanied by an additional kinetic effect due to supersaturation of water vapor (Dütsch et al., 2017, Xia et al., 2023). Vapor at cloud height is typically depleted in heavy isotopes compared to near-surface atmospheric water vapor due to Rayleigh fractionation processes (Giménez et al., 2021 and references therein; Salmon et al., 2019; Sodemann et al., 2017). As raindrops fall through the air column, they continuously exchange water molecules with the surrounding vapour and equilibrate isotopically. This is the basis for the isotopic equilibrium assumption between precipitation and near-surface atmospheric water vapor. During convective storms in warm atmosphere or during precipitation events in dry atmosphere additional fractionating processes occur. During convection storms, vertical diffusion and mixing can decrease $\delta^{18}O_P$ and increase d-excess$_P$ and ^{17}O-excess$_P$ relative to $\delta^{18}O_V$, d-excess$_V$ and ^{17}O-excess$_V$ measured at ground level (Risi et al., 2012; Tremoy et al., 2014; Xia et al., 2022). In contrast, raindrop evaporation below the cloud, has the opposite effect (Fig. 7).

At O_3HP during winter months, $\delta^{18}O_V$ is slightly higher than $\delta^{18}O_{Veq}$ and the two snowfall events have the largest $\Delta\delta^{18}O_{Veq\text{-}V}$ (-12.3‰) (Fig. 5). These differences suggest that $\delta^{18}O_V$ at ground level is higher than at the height of rain formation, and that equilibration during raindrop falling is incomplete. Indeed, equilibration rates are hampered under cold conditions, and no equilibration occurs between vapor and solid (Graf et al., 2019). Incomplete equilibration can also occur when low χ in the atmosphere is associated with strong vertical isotopic gradients in atmospheric water vapor, when drops are large or precipitation forms at high altitude (Graf et al., 2019; Penchenat et al., 2020). This incomplete equilibration has little effect on d-excess$_P$ (average deviation -0.8 ± 3.0 ‰) due to the generally small vertical gradients of d-excess$_V$ in the lowermost troposphere (Salmon et al., 2019; Sodemann et al., 2017). Notably, in winter, ^{17}O-excess$_P$ is always close to ^{17}O-excess$_V$ rather than 10–15 per meg lower as expected from isotopic equilibrium (Fig. 5). The reason for this offset remains unclear so far.

During spring and summer months, the systematic correlation between $\Delta\delta^{18}O_{Veq\text{-}V}$, Δd-excess$_{Veq\text{-}V}$ and Δ^{17}O-excess$_{Veq\text{-}V}$ (Fig. 5) suggests the impact of below-cloud re-evaporation. Rain re-evaporation has been found to occur under unsaturated conditions in mid-latitude to tropical regions (Aemisegger et al., 2015; Aemisegger & Sjolte, 2018; Graf et al., 2019; Landais et al., 2010; Mercer et al., 2020). Indeed, positive $\Delta\delta^{18}O_{Veq\text{-}V}$ values at O_3HP occur when RH is lower than 90 %. The fact that there are no isotopic differences in atmospheric water vapor between rainy and non-rainy days (data not shown) implies that sub-cloud rain re-evaporation does not significantly affect near-surface atmospheric water vapor. The contribution of plant transpiration and soil evaporation to the near-surface atmospheric water vapor may emphasize the isotopic disequilibrium between precipitation and atmospheric water vapor during daytime in summer (cf. Sect. 4.3).

At annual scale, the opposing winter and summer monthly $\Delta\delta^{18}O_{Veq\text{-}V}$ values at our study site effectively cancel each other out, so that $\delta^{18}O_{Veq}$ closely approximates $\delta^{18}O_V$ (cf., Voigt et al., 2023). However, this may differ depending on the environmental setting. Significant deviations from isotopic equilibrium at annual scale were observed in monsoonal areas due to rain re-evaporation (Desphande et al., 2010; Landais et al., 2010; Wen et al., 2010), convective activity (Risi et al., 2012; Tremoy et al., 2014; Xia et al., 2022) or in environments with seasonal precipitation, where the isotopic composition of precipitation is not representative for annual average atmospheric water vapor (Tsujimura et al., 2007; Voigt et al., 2021).

4.6 Effect of the weather regimes

The absence of correlation between the weather regimes and the isotopic composition of vapor and precipitation is probably due to the combined influence of multiple moisture sources weakly isotopically contrasted as presented in Section 3.6. In addition, local moisture recycling may further modify the isotopic signal of atmospheric water vapor and, thus, precipitation, as previously suggested for the circum-Mediterranean region (Baldini et al., 2008). It is also possible that the isotopic composition of near-surface atmospheric water vapor differs slightly from that at the precipitation formation height due to ground roughness, convection, mixing processes in the planetary boundary layer (Griffis et al., 2016; Salmon et al., 2019; Tada et al., 2021).

4.7 Accuracy of $^{17}O\text{-excess}_V$ measurements

Although monthly average $d\text{-excess}_v$ measured at the O_3HP is close to estimated $d\text{-excess}_v$ at the oceanic moisture sources, as expected from Rayleigh distillation, monthly average $^{17}O\text{-excess}_V$ is systematically higher by about 15 per meg. This inconsistency may result from an inaccurate ^{17}O-excess average value used for sea water (-5 per meg) in the calculation of $^{17}O\text{-excess}_V$ above the oceanic moisture sources. To date, the dataset of ^{17}O-excess in seawater is limited (Lin et al., 2021; Luz & Barkan, 2010), so that estimates of oceanic $^{17}O\text{-excess}_V$ are not very accurate. Uncertainty in the turbulence coefficient may also contribute to the mismatch between observed $^{17}O\text{-excess}_V$ and model predictions. Increasing the turbulence coefficient reduces the offset but simultaneously worsens the agreement for $d\text{-excess}_V$ and contradicts previous studies (e.g., Gat, 1996; Pfahl & Wernli, 2008; Uemura et al., 2010, Duetsch et al., 2025). It therefore cannot, by itself, explain the discrepancy. More likely, the closure assumption during ocean evaporation does not fully represent actual isotopic fractionation. For example, aerodynamic conditions over oceans and mixing of water vapor from other sources into the marine boundary layer can decouple ^{17}O-excess and d-excess signals (Xia et al., 2023).

A calibration artifact caused by inaccuracies in the mixing ratio dependency functions or a weak matrix effect cannot be completely excluded. However, it is unlikely, as the quality control standard was routinely measured and accurately calibrated (Sect. 2.2). In any case, such effects would introduce systematic biases and would not alter the main conclusions presented here.

5 Conclusion

This study provides a unique dataset of the triple oxygen and hydrogen isotopic composition of atmospheric water vapor and precipitation in a Mediterranean oak forest ecosystem, highlighting seasonal and diurnal variability and their underlying drivers. Our findings demonstrate the strong potential of ^{17}O-excess as a complementary tracer for disentangling fractionation processes and providing complementary hydrological insights.

The Western Mediterranean, The NE North Atlantic and the SE North Atlantic are identified as the principal moisture sources for vapor and precipitation at the study site. Theoretically predicted seasonal variations in $d\text{-excess}_V$ and $^{17}O\text{-excess}_V$ over these oceanic moisture sources, driven by changes in RH_{SST}, are preserved in the atmospheric water vapor observed at the study site. In contrast, $\delta^{18}O_V$ is only weakly influenced by source conditions and mainly reflects Rayleigh distillation during air mass transport. Monthly values of $\delta^{18}O_P$, $d\text{-excess}_P$ and $^{17}O\text{-excess}_P$ show a similar seasonal pattern to atmospheric water vapor but are modified in summer due to sub-cloud rain re-evaporation.

Despite these source-related controls on $d\text{-excess}_V$ and $^{17}O\text{-excess}_V$, neither tracer clearly discriminates oceanic moisture source regions or weather regimes at monthly scale, likely due to weak isotopic contrasts between the oceanic moisture sources and frequent mixing of moisture from multiple sources. This result contrasts with previous studies that attributed higher $d\text{-excess}_P$ from Western Mediterranean sources compared to the North Atlantic sources to enhanced kinetic fractionation during evaporation, driven by lower RH_{SST} (Casellas et al., 2019; Celle-Jeanton et al., 2001; Cruz-San Julian et al., 1992; Delattre et

al., 2015; Natali et al., 2021). On the other hand, we do observe lower $\delta^{18}O_P$ from North Atlantic sources compared to the Western Mediterranean sources, consistent with earlier observations (Casellas et al., 2019; Celle-Jeanton et al., 2001; Cruz-San Julian et al., 1992; Delattre et al., 2015; Natali et al., 2021). This difference is likely related to enhanced rainout along the longer air mass transport pathway from the North Atlantic. Overall, these findings imply that long-term precipitation isotopic records of precipitation preserved in Mediterranean continental paleoclimate archives should be interpreted with caution when inferring shifts in moisture source regions.

On the diurnal scale, our results demonstrate that $^{17}O\text{-excess}_V$ exhibits a similar diurnal pattern as observed previously for d-excess$_V$ in different environmental settings. Increases in $^{17}O\text{-excess}_V$ and d-excess$_V$ during daytime likely reflect the combination of vegetation-related processes, including soil water and dewfall evaporation, plant transpiration and entrainment of a remnant of the convective boundary layer of the previous day. Nighttime decreases in both tracers likely result from continued isotopic exchange between leaf water, evaporated surface soil water, and ambient water vapor. These findings highlight the strong control of local evapotranspiration processes on sub-daily variability of $^{17}O\text{-excess}_V$ and d-excess$_V$. However, such effects are not evident in monthly $^{17}O\text{-excess}_V$ and d-excess$_V$ as opposing day- and nighttime contributions largely offset each other at the daily scale. This study opens new avenues for investigating land-atmosphere water exchange across diverse climates, vegetation types and timescales.

At the process scale, summer precipitation shows strong coupling between $\delta^{18}O_P$, $^{17}O\text{-excess}_P$ and d-excess$_P$, indicating rain re-evaporation. In contrast, negative $\Delta\delta^{18}O_{Veq\text{-}V}$ values in winter suggest incomplete isotopic equilibration with ambient vapor. Although precipitation often deviates from isotopic equilibrium with near-surface atmospheric water vapor at the event scale, equilibrium water vapor reliably approximates the near-surface isotopic composition of atmospheric water vapor at monthly or annual scale. These findings have important consequences 1) for reconstructing the isotopic composition of atmospheric water vapor to constrain hydrological models of evaporative fractionation when direct measurements are not available, and 2) for simulating the isotopic composition of precipitation in isotope-enabled climate models. Our results support the robustness of reconstructions assuming isotopic equilibrium at annual scales in this climate context. However, at daily- to event scales, accurate reconstruction of the isotopic composition of atmospheric water vapor and simulation of rainfall formation require accounting for post-condensation processes, such as raindrop re-evaporation and rain-vapor equilibration during raindrop fall through the atmospheric column. When process scale dynamics are targeted, simultaneous measurements of triple oxygen and hydrogen isotopes in precipitation and atmospheric water vapor are essential across diverse environmental settings to further constrain and improve the representation of these processes in isotope-enabled models.

Appendices

Appendix A

Table A1: Run architectures used for calibrations of atmospheric water vapor measurements.

Working standard	Number of injections	Water mixing ratio (ppmv)	Purpose	Data processing
JAN – MAY 2021				
ICE	20	22000	Conditioning	discard
ICE	10	17000	Validation of mixing ratio dependency function	discard first 5, average last 5
ICE	10	11000	Validation of mixing ratio dependency function, VSMOW-SLAP calibration	discard first 5, average last 5
ICE	10	6000	Validation of mixing ratio dependency function	discard first 5, average last 5
ICE	10	3500	Validation of mixing ratio dependency function	discard first 5, average last 5
NOC	10	22000	conditioning	discard first 5, average last 5
NOC	10	17000	Validation of mixing ratio dependency function	discard first 5, average last 5
NOC	10	11000	Validation of mixing ratio dependency function, VSMOW-SLAP calibration	discard first 5, average last 5
NOC	10	6000	Validation of mixing ratio dependency function	discard first 5, average last 5
NOC	10	3500	Validation of mixing ratio dependency function	discard first 5, average last 5
TAP	10	22000	Conditioning	discard first 5, average last 5
TAP	10	17000	Validation of mixing ratio dependency function	discard first 5, average last 5
TAP	10	11000	Validation of mixing ratio dependency function, VSMOW-SLAP calibration	discard first 5, average last 5
TAP	10	6000	Validation of mixing ratio dependency function	discard first 5, average last 5
TAP	10	3500	Validation of mixing ratio dependency function	discard first 5, average last 5
JUN – OCT 2021				
ICE	20	28000	Conditioning	discard
ICE	8	11000	VSMOW-SLAP calibration	discard first 2, average last 6
NOC	15	28000	Conditioning	discard
NOC	8	11000	VSMOW-SLAP calibration	discard first 2, average last 6
TAP	15	28000	Conditioning	discard
TAP	8	11000	VSMOW-SLAP calibration	discard first 2, average last 6
NOV – DEC 2021				
ICE	20	28000	Conditioning	discard
ICE	8	11000	Validation of mixing ratio dependency function, VSMOW-SLAP calibration	discard first 2, average last 6
ICE	8	5000	Validation of mixing ratio dependency function	discard first 2, average last 6
NOC	15	28000	Conditioning	discard
NOC	8	11000	Validation of mixing ratio dependency function, VSMOW-SLAP calibration	discard first 2, average last 6

NOC	8	5000	Validation of mixing ratio dependency function	discard first 2, average last 6
TAP	15	28000	Conditioning	discard
TAP	8	11000	Validation of mixing ratio dependency function, VSMOW-SLAP calibration	discard first 2, average last 6
TAP	8	5000	Validation of mixing ratio dependency function	discard first 2, average last 6

620

Table A2: Means (AV) and standard deviations (SD) of coefficients of mixing ratio dependency functions for $\delta^{17}O$, $\delta^{18}O$ and $\delta^{2}H$ of the three used standards (ICE: $\delta^{17}O$ = -14.2404 ‰, $\delta^{18}O$ = -26.8485 ‰, $\delta^{2}H$ = -203.76 ‰; NOC: $\delta^{17}O$ = -8.9619 ‰, $\delta^{18}O$ = -16.9109‰, $\delta^{2}H$ = -125.69‰;, TAP: $\delta^{17}O$ = -4.5397 ‰, $\delta^{18}O$ = -8.6382 ‰, $\delta^{2}H$ = -59.24‰). The mixing ratio dependency functions have the form f(x) = a/x+bx+c and are determined relative to a water mixing ratio of 10000 ppmv.

Coefficient	$\delta^{17}O$		$\delta^{18}O$		$\delta^{2}H$	
	AV	SD	AV	SD	AV	SD
ICE						
a	9.37E+02	7.41E+01	1.12E+03	1.01E+02	8.89E+03	4.23E+02
b	3.46E-06	4.72E-07	1.01E-05	8.32E-07	1.12E-05	4.66E-06
c	-1.26E-01	1.37E-02	-2.15E-01	2.16E-02	-1.01E+00	1.15E-01
NOC						
a	6.77E+02	5.60E+01	6.67E+02	9.08E+01	5.27E+03	6.72E+02
b	3.00E-06	7.07E-07	9.44E-06	1.10E-06	1.47E-05	5.94E-06
c	-9.84E-02	1.53E-02	-1.64E-01	2.46E-02	-6.42E-01	1.65E-01
TAP						
a	2.95E+02	9.14E+01	-2.68E+01	1.22E+02	1.62E+02	5.79E+02
b	3.75E-06	6.22E-07	1.05E-05	9.79E-07	1.88E-05	6.98E-06
c	-6.54E-02	1.85E-02	-1.00E-01	2.60E-02	-2.05E-01	1.61E-01

625

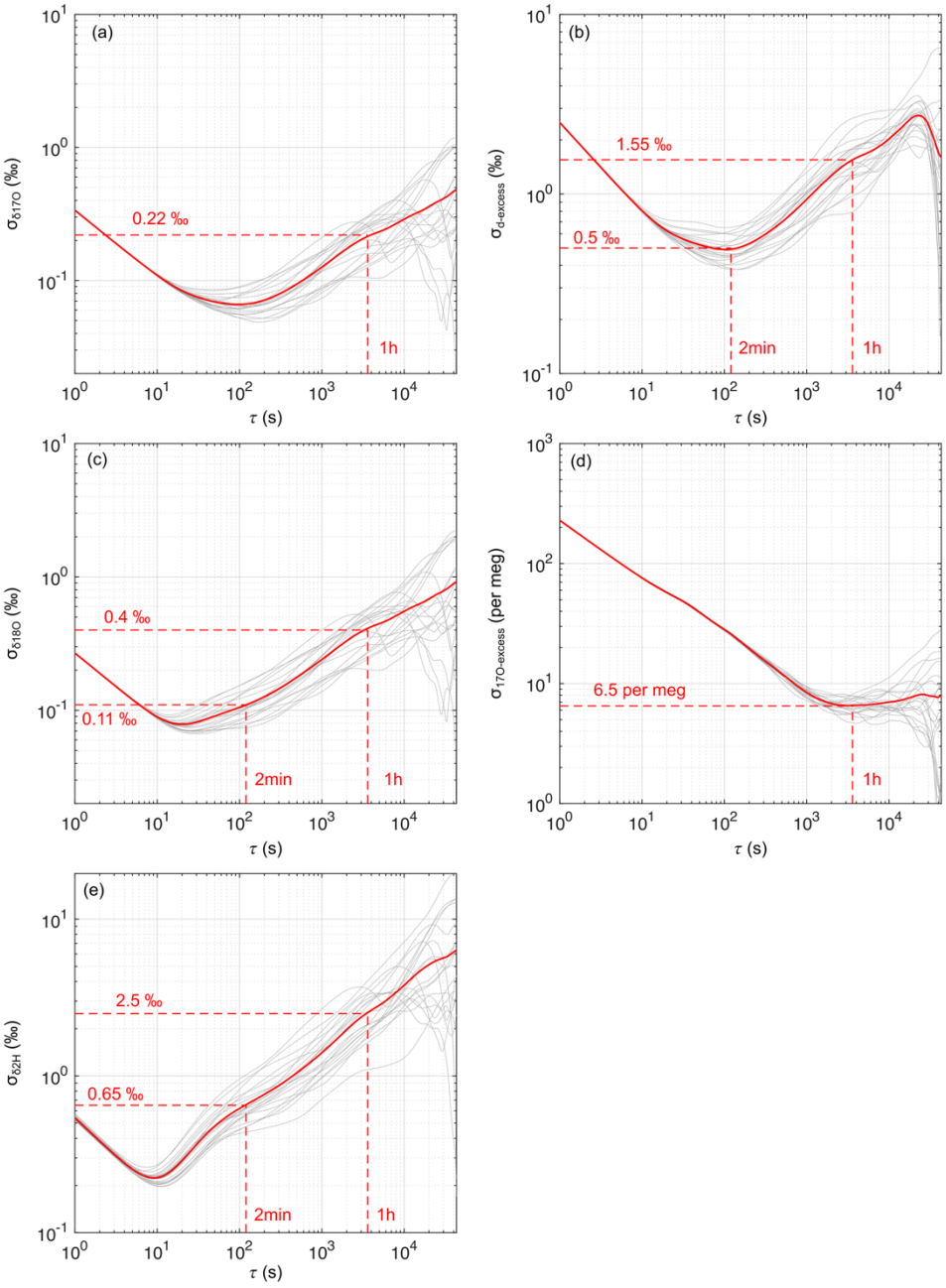

Fig. A1: Allan deviations σ for (a) $\delta^{17}O$, (c) $\delta^{18}O$, (e) $\delta^{2}H$, (b) d-excess and (d) ^{17}O-excess for 24-hour records of atmospheric water vapor at O_3HP gathered between June 1, 2021 and June 30, 2021. The red solid curve illustrates the mean Allan deviations. Dashed lines and associated numbers indicate the Allan deviation for 1 hour and 2 min averaging time, respectively.

630

Appendix B

Table B1: Sample name, sample type, sampling date and isotopic composition of meteoric waters collected in this study. Samples from springs, wells and rivers in the surroundings of the study site were collected seasonally. Precipitation was collected monthly from June 2019 to December 2020, but on quasi-event scale in 2021. Given isotopic values for precipitation in 2021 represent amount-weighted monthly averages. In addition, the amount-weighted average isotopic values and standard deviations for precipitation in 2020, 2021 and over the whole dataset are given.

Sample name	Sample type	Sampling date	$\delta^{18}O$ (‰)	$\delta'^{18}O$ (‰)	$\delta^{2}H$ (‰)	^{17}O-excess (per meg)	d-excess (‰)	Precipitation amount (mm)
Lavoir Barri	spring	Dec-20	-7.8	-7.8	-50.3	33	11.7	–
Lavoir Barri	spring	Apr-21	-7.7	-7.7	-49.8	37	11.9	–
Lavoir Barri	spring	Jun-21	-7.7	-7.7	-49.8	28	11.9	–
Lavoir Barri	spring	Aug-21	-7.7	-7.8	-50.2	28	11.8	–
Lavoir Barri	spring	Oct-21	-7.7	-7.8	-50.1	26	11.9	–
Lavoir Marceline	spring	May-20	-7.2	-7.2	-47.3	27	10.4	–
Lavoir Marceline	spring	Dec-20	-7.4	-7.4	-48.1	33	11.1	–
Lavoir Marceline	spring	Apr-21	-7.4	-7.5	-48.3	32	11.1	–
Lavoir Marceline	spring	Jun-21	-7.4	-7.4	-47.8	37	11.2	–
Lavoir Marceline	spring	Aug-21	-7.4	-7.4	-48.0	20	11.1	–
Lavoir Marceline	spring	Oct-21	-7.0	-7.0	-45.1	26	10.9	–
Puits jardin	well	Dec-20	-7.2	-7.2	-46.4	27	11.1	–
Puits jardin	well	Apr-21	-7.2	-7.2	-46.8	28	10.7	–
Puits jardin	well	Jun-21	-7.0	-7.1	-45.8	30	10.6	–
Puits jardin	well	Aug-21	-7.0	-7.1	-45.8	26	10.5	–
Puits jardin	well	Oct-21	-6.9	-6.9	-45.1	27	10.3	–
Source enterrée	spring	Dec-20	-6.1	-6.1	-38.4	33	10.2	–
Source enterrée	spring	Jun-21	-7.4	-7.4	-46.9	33	12.5	–
Source enterrée	spring	Aug-21	-7.3	-7.3	-45.9	20	12.2	–
Source enterrée	spring	Oct-21	-5.8	-5.9	-35.8	23	11.0	–
Riviere Largue	river	May-20	-7.3	-7.4	-47.1	34	11.6	–
Riviere Largue	river	Dec-20	-7.5	-7.5	-48.7	28	11.1	–
Riviere Largue	river	Apr-21	-7.5	-7.6	-49.0	26	11.2	–
Riviere Largue	river	Jun-21	-7.5	-7.6	-48.7	27	11.5	–
Riviere Largue	river	Aug-21	-7.4	-7.4	-48.3	22	11.1	–
Riviere Largue	river	Oct-21	-7.3	-7.3	-47.4	30	11.1	–
AV			**-7.3**		**-47.0**	**29**	**11.2**	–
SD			0.5		3.3	5	0.6	–
O_3HP	precipitation	Jun-19	-3.6	-3.6	-26.2	14	2.3	15
O_3HP	precipitation	Jul-19	-1.1	-1.1	-6.5	-1	2.3	64
O_3HP	precipitation	Aug-19	–	–	–	–	–	0
O_3HP	precipitation	Sep-19	-6.6	-6.6	-45.6	20	6.9	87
O_3HP	precipitation	Oct-19	-6.1	-6.1	-35.6	22	12.9	200
O_3HP	precipitation	Nov-19	-9.0	-9.0	-60.8	25	11.0	392
O_3HP	precipitation	Dec-19	-9.2	-9.2	-63.8	34	9.8	124
O_3HP	precipitation	Jan-20	-6.7	-6.7	-42.5	34	10.8	24
O_3HP	precipitation	Feb-20	–	–	–	–	–	0
O_3HP	precipitation	Mar-20	-7.0	-7.0	-49.3	29	6.8	39
O_3HP	precipitation	Apr-20	-5.5	-5.5	-32.2	29	12.0	40
O_3HP	precipitation	May-20	-6.4	-6.4	-41.3	20	9.9	150
O_3HP	precipitation	Jun-20	-5.1	-5.1	-35.4	14	5.2	65
O_3HP	precipitation	Jul-20	–	–	–	–	–	0
O_3HP	precipitation	Aug-20	-2.9	-2.9	-15.9	2	7.5	8
O_3HP	precipitation	Sep-20	-7.1	-7.1	-47.8	19	9.1	37
O_3HP	precipitation	Oct-20	-4.6	-4.6	-23.4	26	13.1	25
O_3HP	precipitation	Nov-20	-7.6	-7.7	-49.8	25	11.2	33
O_3HP	precipitation	Dec-20	-11.8	-11.9	-78.8	32	15.6	71
O_3HP	precipitation	Jan-21	-10.4	-10.4	-71.2	34	11.6	53
O_3HP	precipitation	Feb-21	-8.8	-8.8	-60.1	28	9.9	40
O_3HP	precipitation	Mar-21	-4.2	-4.2	-21.8	30	12.0	9
O_3HP	precipitation	Apr-21	-8.0	-8.0	-52.1	26	12.0	125
O_3HP	precipitation	May-21	-5.8	-5.8	-33.3	30	12.9	82

O_3HP	precipitation	Jun-21	-5.6	-5.6	-37.1	26	7.8	13
O_3HP	precipitation	Jul-21	-7.6	-7.6	-62.3	9	-1.4	21
O_3HP	precipitation	Aug-21	-7.0	-7.0	-47.9	5	8.2	58
O_3HP	precipitation	Sep-21	-5.7	-5.7	-36.2	14	9.2	70
O_3HP	precipitation	Oct-21	-3.3	-3.3	-8.2	28	18.2	85
O_3HP	precipitation	Nov-21	-8.6	-8.6	-55.8	41	12.8	85
O_3HP	precipitation	Dec-21	-11.1	-11.2	-78.5	30	10.6	88
amount-weighted AV		**2020**	**-7.0**		**-45.6**	**23**	**10.2**	**492**
amount-weighted SD			2.2		15.4	7	3.1	
amount-weighted AV		**2021**	**-7.5**		**-48.1**	**27**	**11.6**	**730**
amount-weighted SD			2.3		20.2	9	3.5	
amount-weighted AV		**ALL**	**-7.3**		**-48.1**	**24**	**10.6**	**2104**
amount-weighted SD			2.3		17.7	8	3.3	

Table B2: Monthly and annual average isotopic composition of atmospheric water vapor at 12.5 m agl (V) and water vapor estimated from isotopic equilibrium with monthly amount-weighted precipitation data (V_{eq}) for the period from January to December 2021.

Month	**$\delta^{18}O_V$ (‰)**		**$\delta^{2}H_V$ (‰)**		**d-excess$_V$ (‰)**		**^{17}O-excess$_V$ (per meg)**		**$\delta^{18}O_{Veq}$ (‰)**		**$\delta^{2}H_{Veq}$ (‰)**		**d-excess$_{Veq}$ (‰)**		**^{17}O-excess$_{Veq}$ (per meg)**	
	AV	**SD**	**AV**	**SD**	**AV**	**SD**	**AV**	**SD**	**AV**	**SD**	**AV**	**SD**	**AV**	**SD**	**AV**	**SD**
Jan	-23.6	4.4	-174	32	14.6	4.7	40	10	-21.5	4.9	-161	39	11.7	2.1	23	12
Feb	-17.5	3.7	-126	30	13.9	5.2	25	7	-19.5	4.0	-145	32	10.4	3.0	17	7
Mar	-17.3	3.2	-125	24	13.3	3.0	24	10	-15.0	–	-110	–	9.5	–	19	–
Apr	-17.2	2.5	-122	19	15.5	3.8	30	10	-18.6	1.0	-137	7	12.2	3.4	16	6
May	-16.3	2.1	-119	17	11.7	2.5	26	4	-16.0	1.0	-116	11	12.8	6.0	20	2
Jun	-14.6	2.3	-105	18	11.9	1.9	27	6	-15.3	2.4	-112	18	9.9	2.9	16	7
Jul	-16.2	2.3	-118	17	11.6	1.3	25	4	-17.1	2.5	-134	20	2.9	1.6	0	3
Aug	-16.0	2.3	-116	17	12.6	1.6	26	6	-16.5	0.8	-121	7	11.4	0.2	-4	9
Sep	-15.7	1.9	-112	15	13.7	1.7	32	4	-15.4	1.5	-113	8	10.8	4.4	4	8
Oct	-15.7	1.5	-109	12	16.7	1.9	38	9	-13.6	0.3	-93	2	16.0	0.6	18	2
Nov	-20.6	3.2	-149	24	16.1	2.5	26	12	-19.3	1.7	-142	15	12.9	2.9	30	6
Dec	-22.1	3.4	-163	26	14.3	2.8	35	8	-22.0	2.5	-164	22	12.1	2.1	19	6
Annual AV	**-17.7**	**2.8**	**-128**	**22**	**13.8**	**1.7**	**30**	**5**	**-17.8**	**2.7**	**-130**	**22**	**12.3**	**3.1**	**16**	**10**

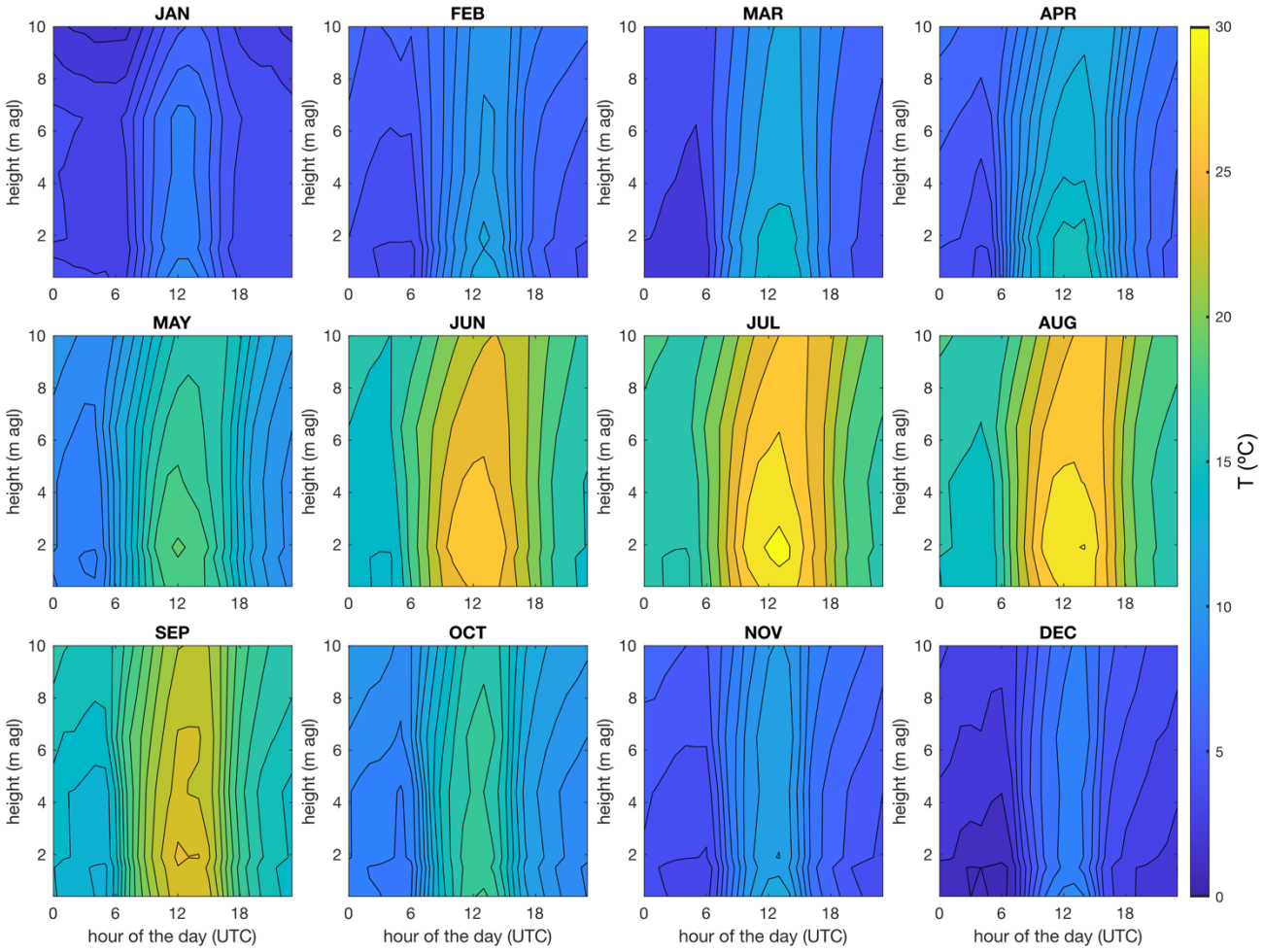

Figure B1: Monthly average variability of atmospheric temperature in the near-surface atmosphere over the day. Temperature measurements at 0.4 m, 1.5 m, 1.9 m, 4.4 m 6.15 m and 10 m agl were obtained from the O_3HP database (Reiter et al., 2015). Data were linearly interpolated between measurement heights, and the hourly means were computed for each month.

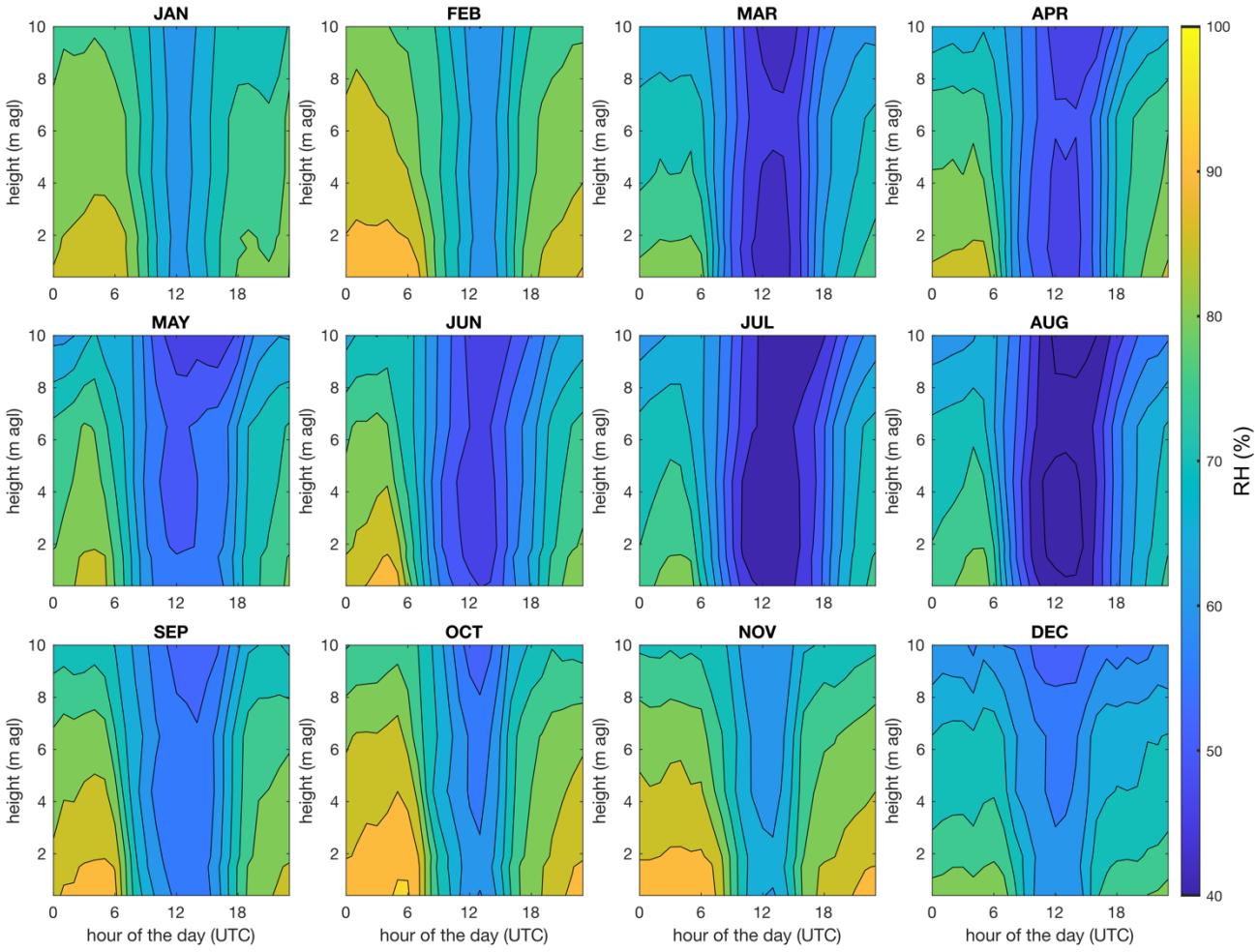

Figure B2: Monthly average variability of atmospheric relative humidity in the near-surface atmosphere over the day. Relative humidity measurements at 0.4 m, 1.5 m, 1.9 m, 4.4 m 6.15 m and 10 m agl were obtained from the O_3HP database (Reiter et al., 2015). Data were linearly interpolated between measurement heights, and the hourly means were computed for each month.

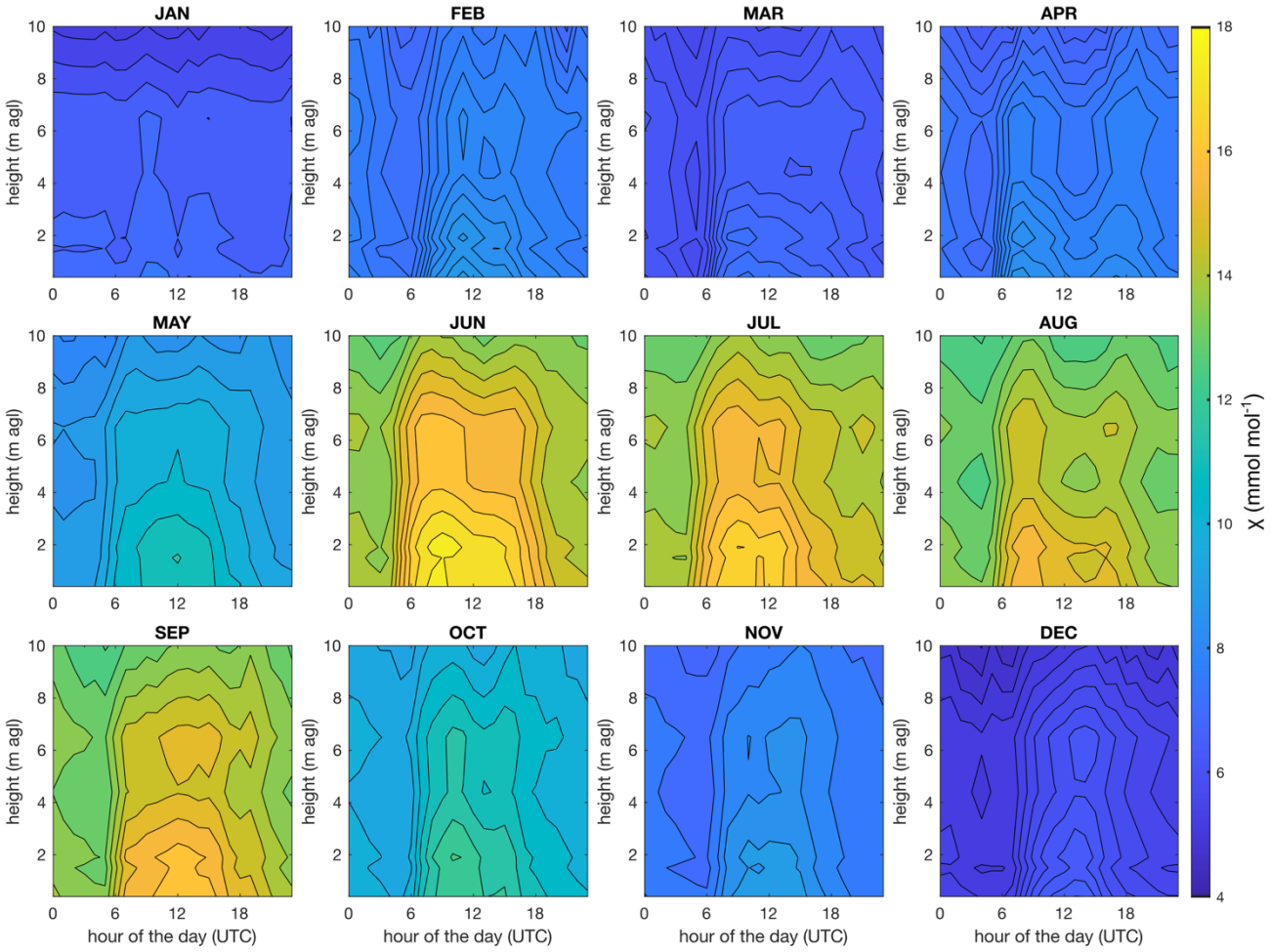

Figure B3: Monthly average variability of the atmospheric water mixing ratio in the near-surface atmosphere over the day. Measurements of atmospheric temperature and relative humidity at 0.4 m, 1.5 m, 1.9 m, 4.4 m 6.15 m and 10 m agl were obtained from the O_3HP database (Reiter et al., 2015). The atmospheric water mixing ratio was calculated from these data, linearly interpolated between heights, and averaged hourly for each month.

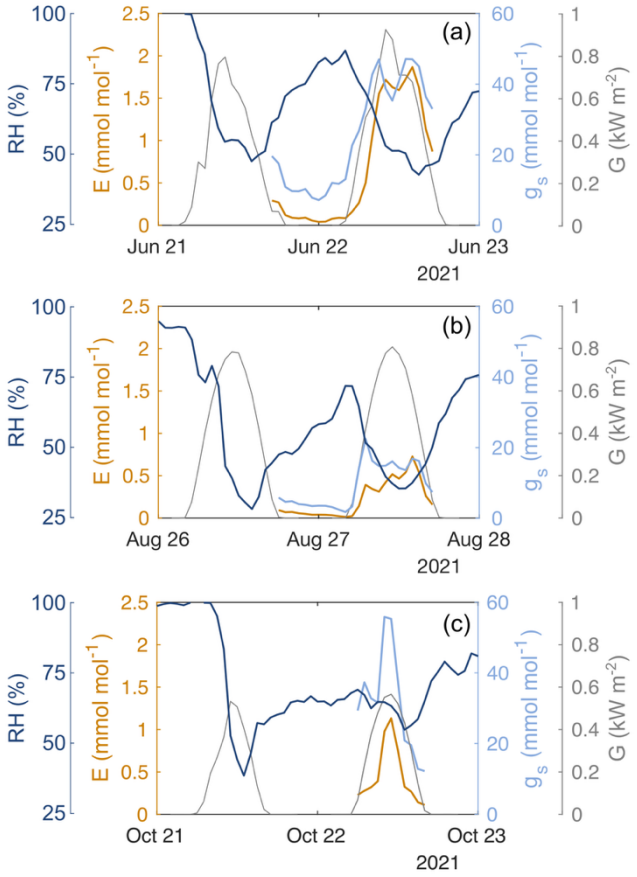

Figure B4: Diurnal evolution of transpiration (E) and stomatal conductance (g_s) of individual oak leaves in the sun-crown of the forest canopy in different stages of the oak forest growing season: (a) early stage, (b) dry stage, (c) last stage. The diurnal cycle of global solar radiation (G, grey curve) and relative humidity (RH) are shown for comparison.

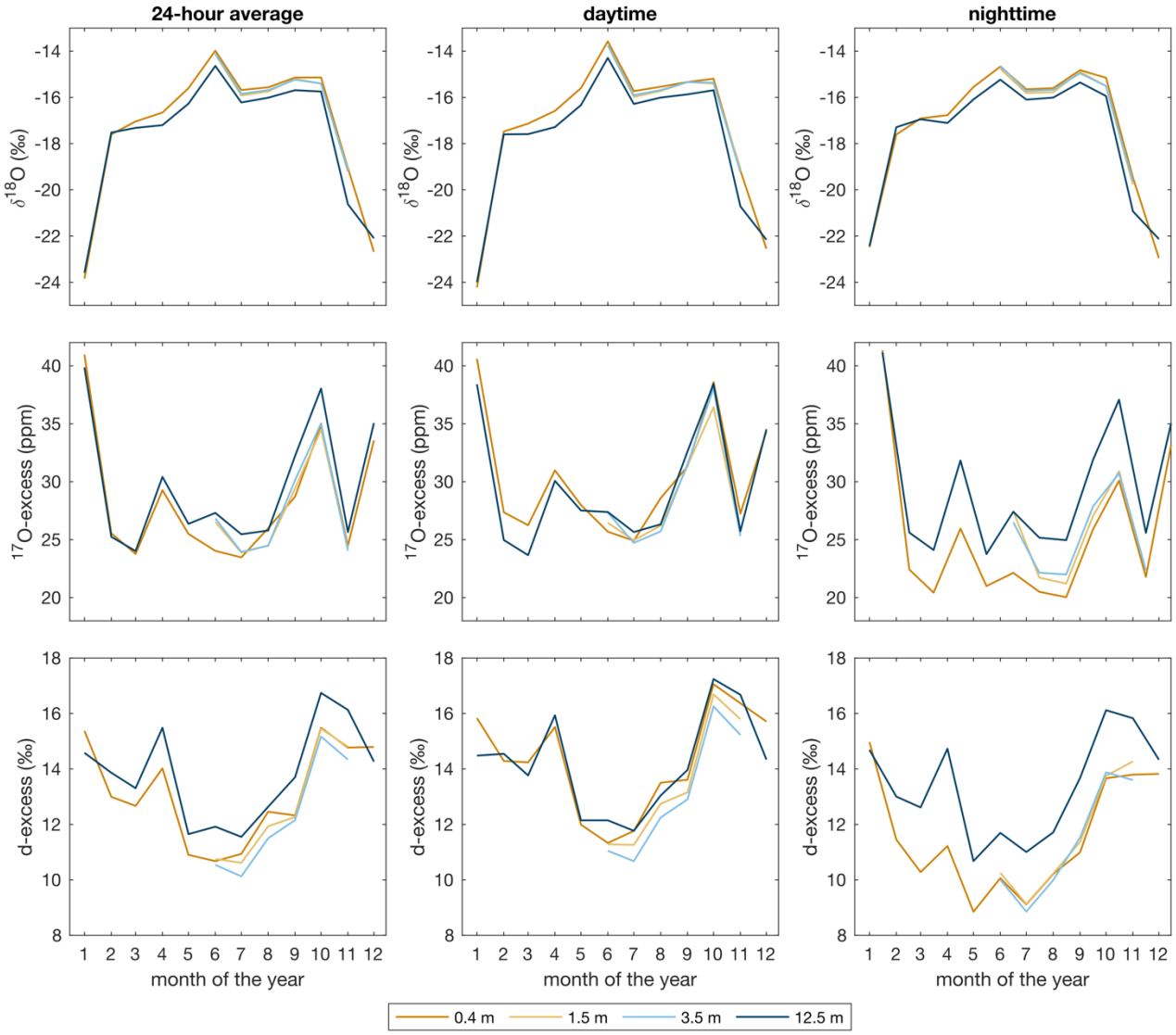

Figure B5: Monthly average of $\delta^{18}O$, ^{17}O-excess and d-excess of atmospheric water vapor at different heights above ground level (agl) in 2021 for daily, daytime and night-time conditions. Atmospheric water vapor at 1.5 and 3.5 m agl was monitored continuously only from June to November 2021, in relation to the oak forest growing season. Therefore, for these heights no isotopic data is available from January to May and December 2021.

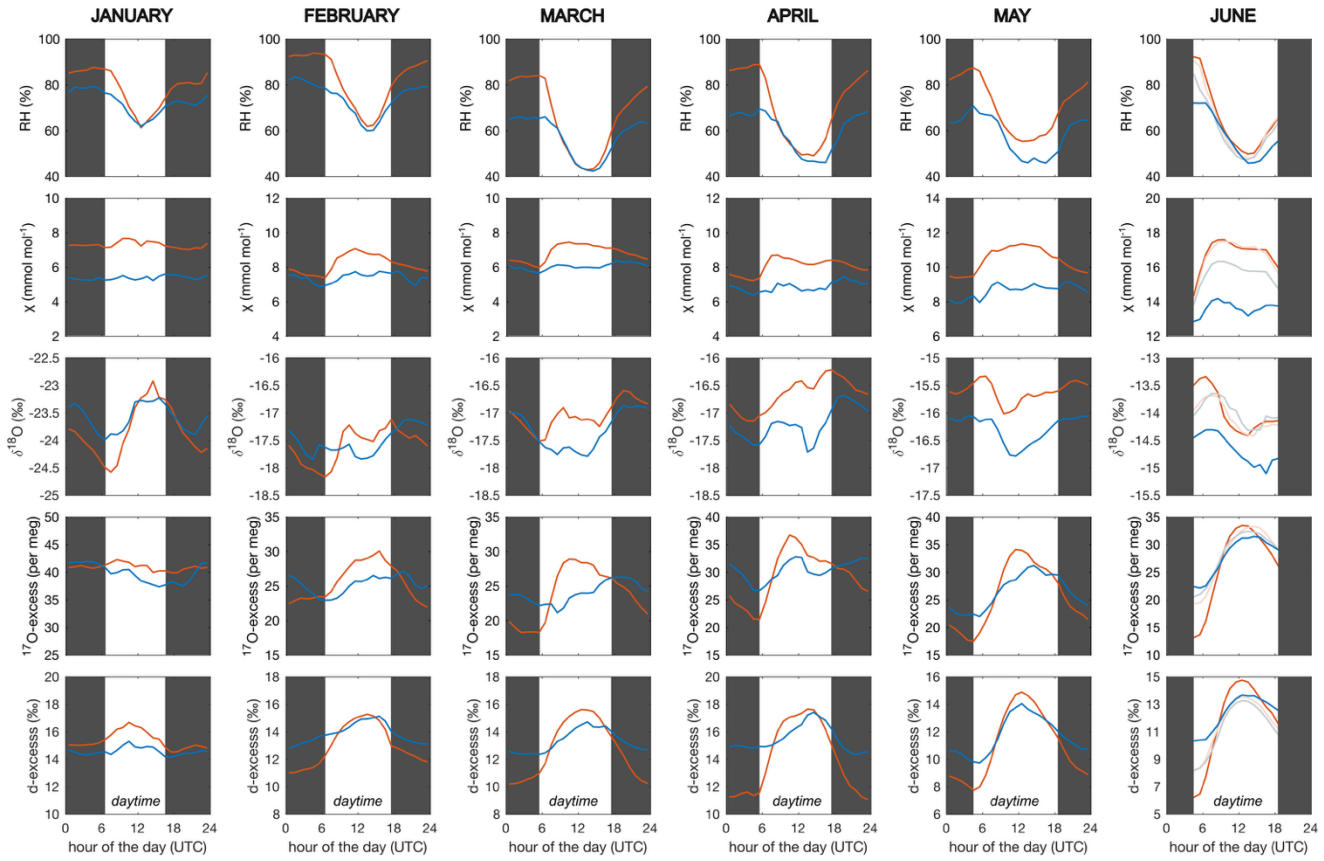

Figure B6: Monthly average diurnal cycle of relative humidity (RH), atmospheric water mixing ratio (χ) and $\delta^{18}O$, d-excess and ^{17}O-excess of atmospheric water vapor at different measurements heights above the grass plot (red) and below (pale), within (grey) and above (blue) the oak forest canopy for January to June 2021. The grey shaded areas indicate the night-time periods.

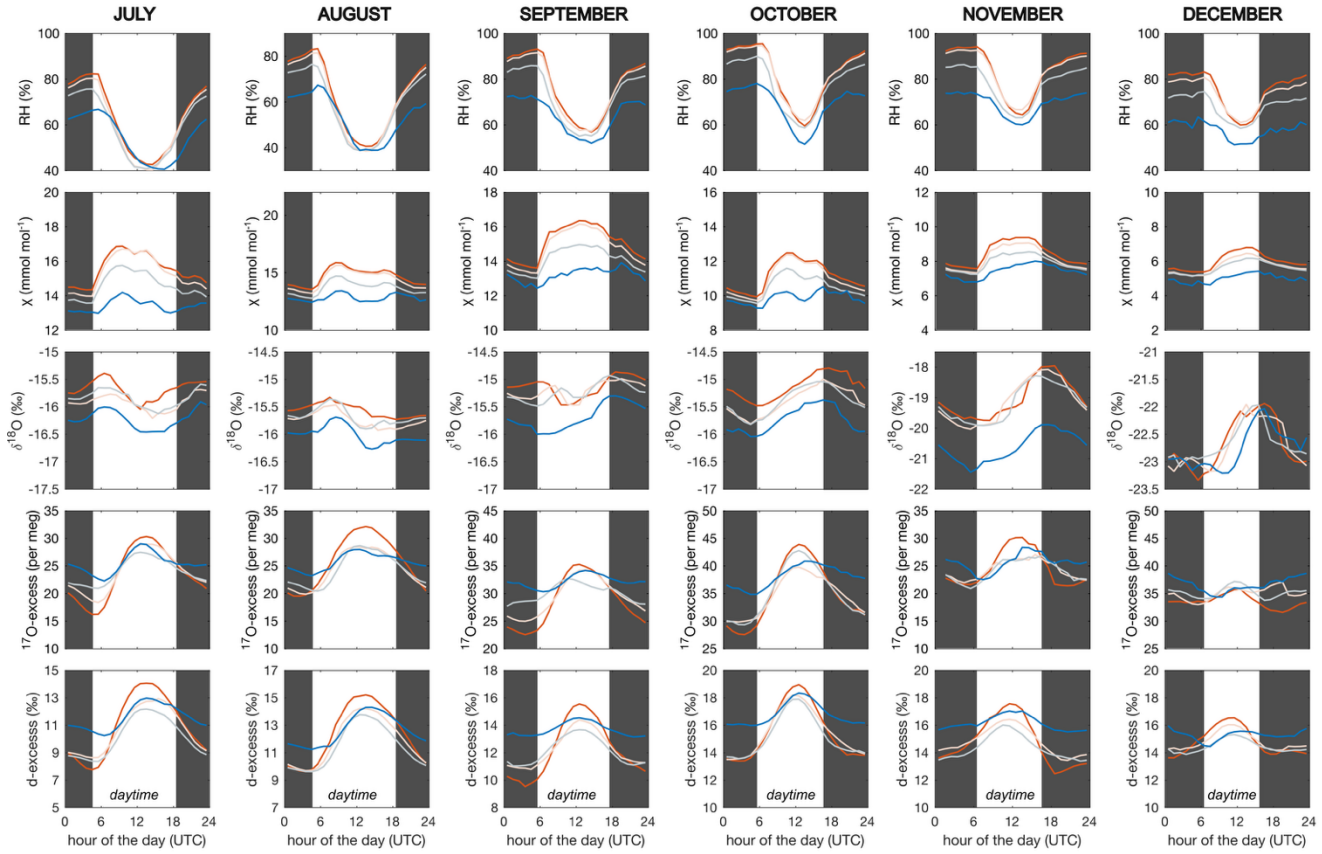

Figure B7: Same as Figure B6, but for July to December 2021.

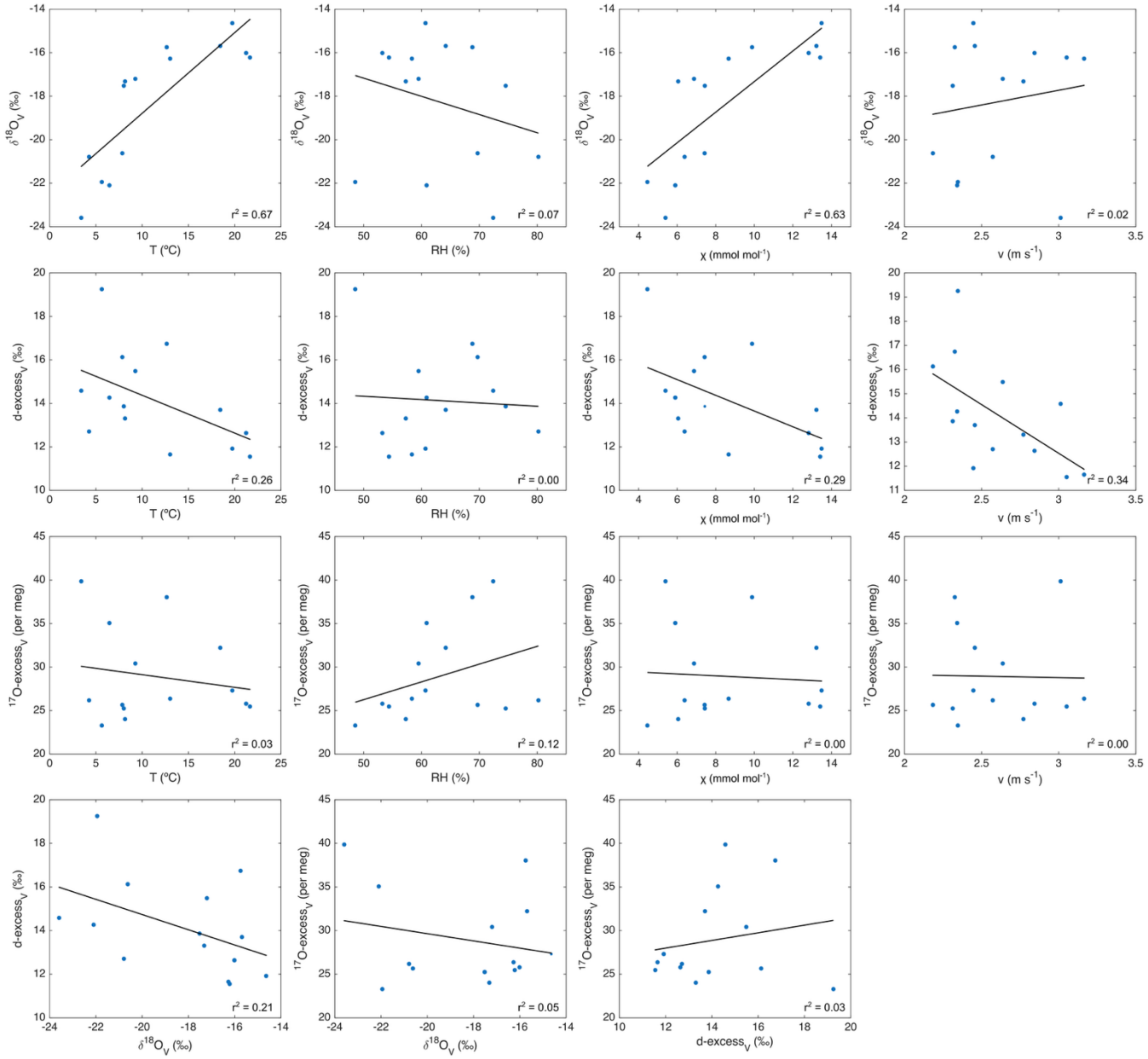

680 **Figure B8:** Correlations observed between monthly average $\delta^{18}O$, d-excess and ^{17}O-excess of atmospheric water vapor measured at 12.5 m agl and relative humidity (RH), atmospheric temperature (T_{air}), the atmospheric water mixing ratio (χ) and wind speed (v) at 10 m agl.

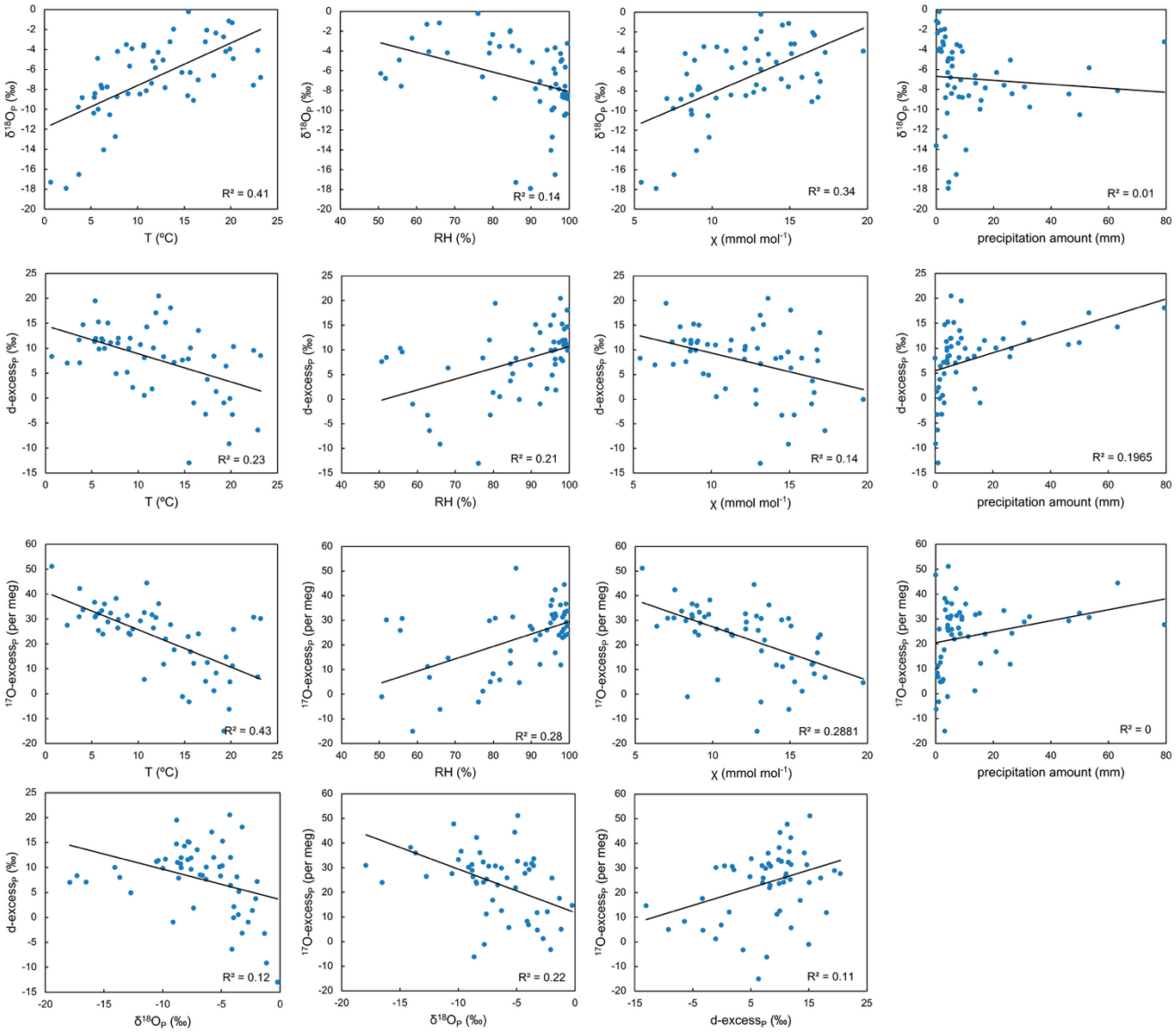

Figure B9: Correlations observed between event-based $\delta^{18}O$, d-excess and ^{17}O-excess of precipitation and relative humidity (RH), atmospheric temperature (T_{air}), the atmospheric water mixing ratio (χ) and precipitation amount.

685

690

Appendix C

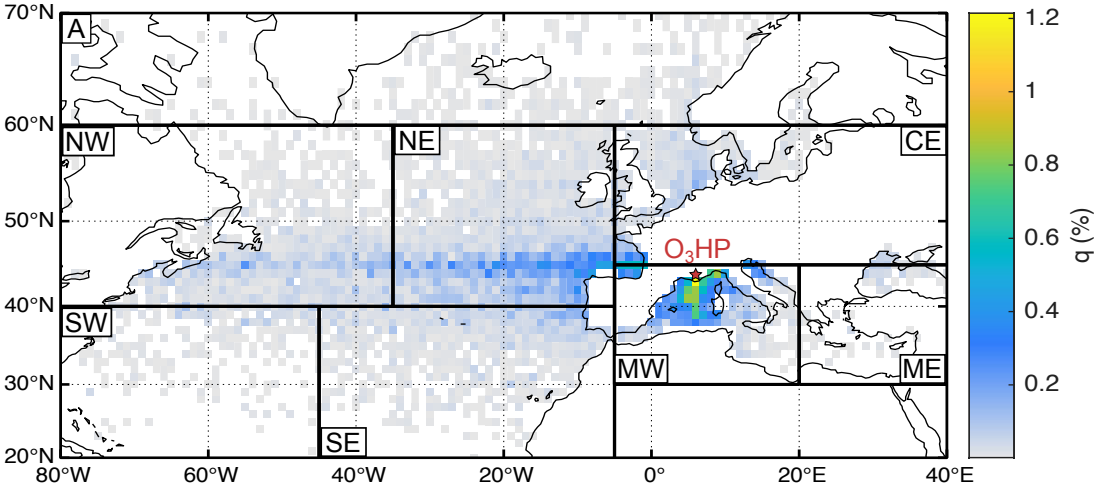

Figure C1: Annual mean oceanic moisture source contributions to atmospheric water vapor at O_3HP. Shading: Relative contribution of evaporation from respective grid cell to the final specific humidity of each trajectory.

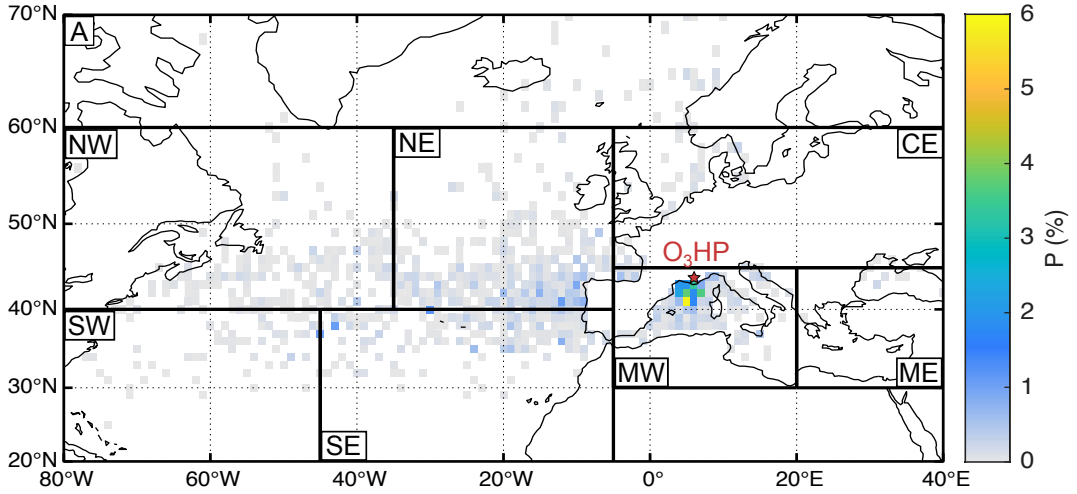

Figure C2: Annual mean oceanic moisture source contributions to precipitation at O_3HP. Shading: Relative contribution of evaporation from respective grid cell to diagnosed precipitation at O_3HP.

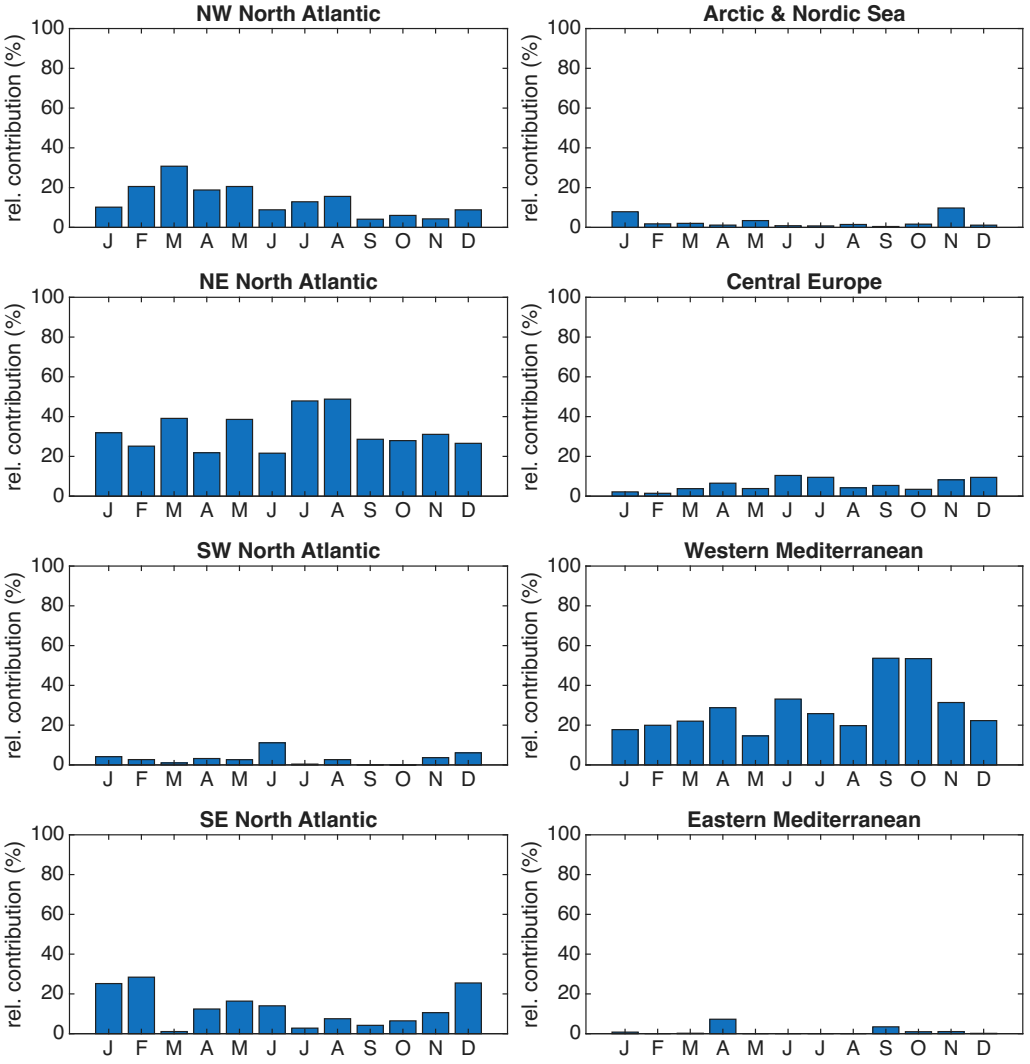

Figure C3: Relative contributions from the eight oceanic moisture source regions (% of final specific humidity).

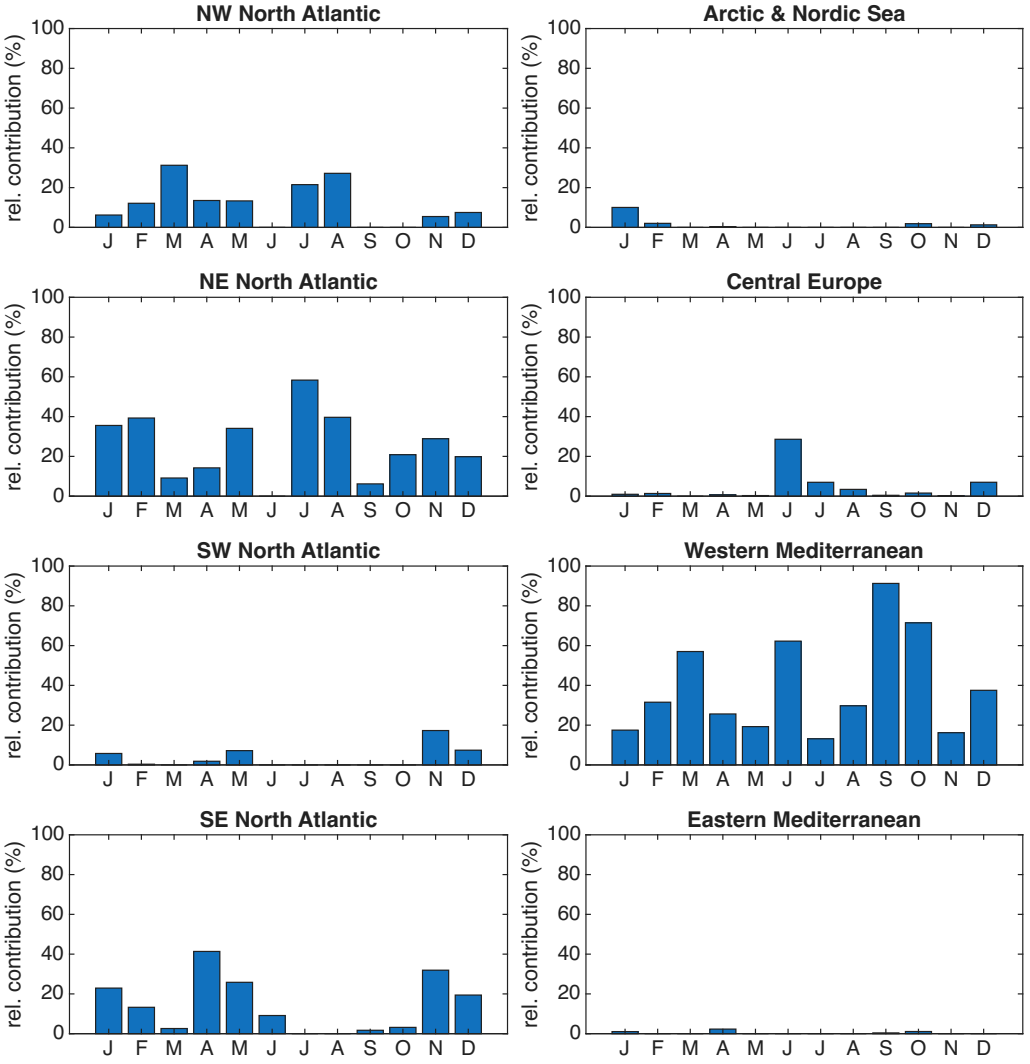

Figure C4: Relative contributions from the eight oceanic moisture source regions (% of accounted precipitation).

Table C1: Isotopic composition of atmospheric water vapor derived from the eight defined oceanic moisture source regions.

Moisture source region	$\delta^{18}O_V$ (‰)		d-excess$_V$ (‰)		^{17}O-excess$_V$ (per meg)		relative contribution to on-site moisture (%)
	AV	SD	AV	SD	AV	SD	
NW North Atlantic	-15.8	4.9	11.8	4.1	26	10	13
NE North Atlantic	-15.5	4.9	11.0	3.8	25	9	33
SW North Atlantic	-14.8	3.7	10.9	2.9	27	9	3
SE North Atlantic	-14.9	6.1	9.4	3.9	27	11	12
Arctic and Nordic Sea	-16.3	8.5	10.8	6.4	25	15	2
Central Europe	-17.7	5.0	12.9	4.0	26	9	6
Western Mediterranean	-14.8	4.9	11.2	3.6	26	9	29
Eastern Mediterranean	-16.6	4.7	13.2	4.7	34	12	1

Table C2: Isotopic composition of precipitation derived from the eight defined oceanic moisture source regions.

Moisture source region	$\delta^{18}O_P$ (‰)		d-excess$_P$ (‰)		^{17}O-excess$_P$ (per meg)		relative contribution to accounted P amount (%)
	AV	SD	AV	SD	AV	SD	
NW North Atlantic	-8.2	2.8	13.5	3.8	31	11	8
NE North Atlantic	-9.2	4.5	11.8	3.8	33	14	25
SW North Atlantic	-8.5	2.3	11.9	2.4	32	4	4
SE North Atlantic	-8.4	2.4	12.0	3.5	32	5	18
Arctic and Nordic Sea	-12.1	6.7	12.9	2.7	42	17	2
Central Europe	-7.5	4.3	10.3	7.9	28	14	2
Western Mediterranean	-7.6	2.9	11.9	3.8	29	7	41
Eastern Mediterranean	-10.0	8.4	11.2	10.1	34	25	1

715

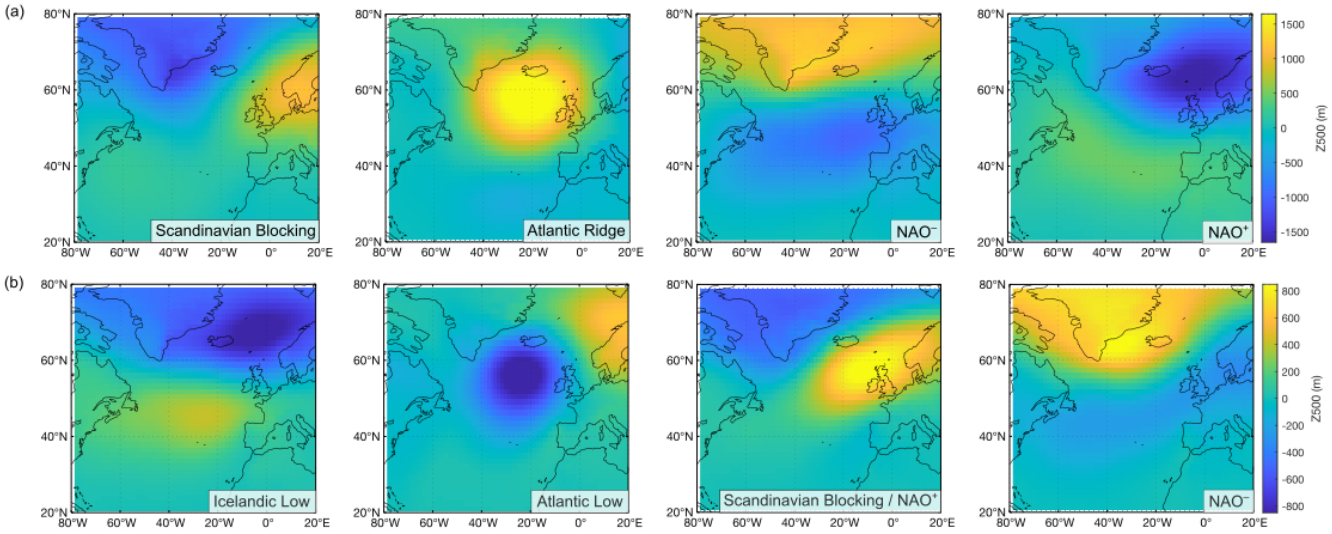

Figure C5: Centroids of (a) the four wintertime and (b) the four summertime weather regimes obtained from daily anomalous geopotential height at the 500-hPa altitude (Z500, colour) from the European Centre for the Medium-Range Weather Forecasts (ECMWF) ERA5 reanalysis over 1989–2022. In winter, the Atlantic Ridge regime is associated with a high-pressure system over the Atlantic Ocean, driving strong northwesterly winds (Mistral) and resulting in cool, dry conditions in the Mediterranean region (Vautard, 1990). The NAO– regime emerges when the Icelandic low shifts southward, displacing the Atlantic jet stream to lower latitudes and inducing southerly winds that bring warmer, wetter conditions to the Mediterranean (Cassou et al., 2004). In contrast, the NAO+ regime is characterized by a strong pressure gradient between the Icelandic Low and the Azores High, promoting westerly to northwesterly winds and generally dry conditions in the Mediterranean (Cassou et al., 2004). The Scandinavian Blocking regime involves a persistent anticyclone over the Scandinavian Peninsula, preventing low pressure systems reaching Europe and leads to north-easterly winds across the western Mediterranean. In summer, the Blocking/NAO+ regime resembles a blocking-like pattern, with a high-pressure anomaly over Scandinavia and the North Sea. The Atlantic Low is dominated by a low-pressure system over the North Atlantic, accompanied by weaker positive anomalies extending toward Scandinavia, facilitating the advection of warm air masses from northern Africa and the Mediterranean basin (Cassou et al., 2005). The summer NAO– regime is characterized by a low-pressure anomaly over the British Isles and a strong high-pressure anomaly over Greenland, while the Icelandic Low regime displays a dipole pattern with a low-pressure anomaly between Iceland and Scandinavia and a weak high-pressure anomaly over the North Atlantic.

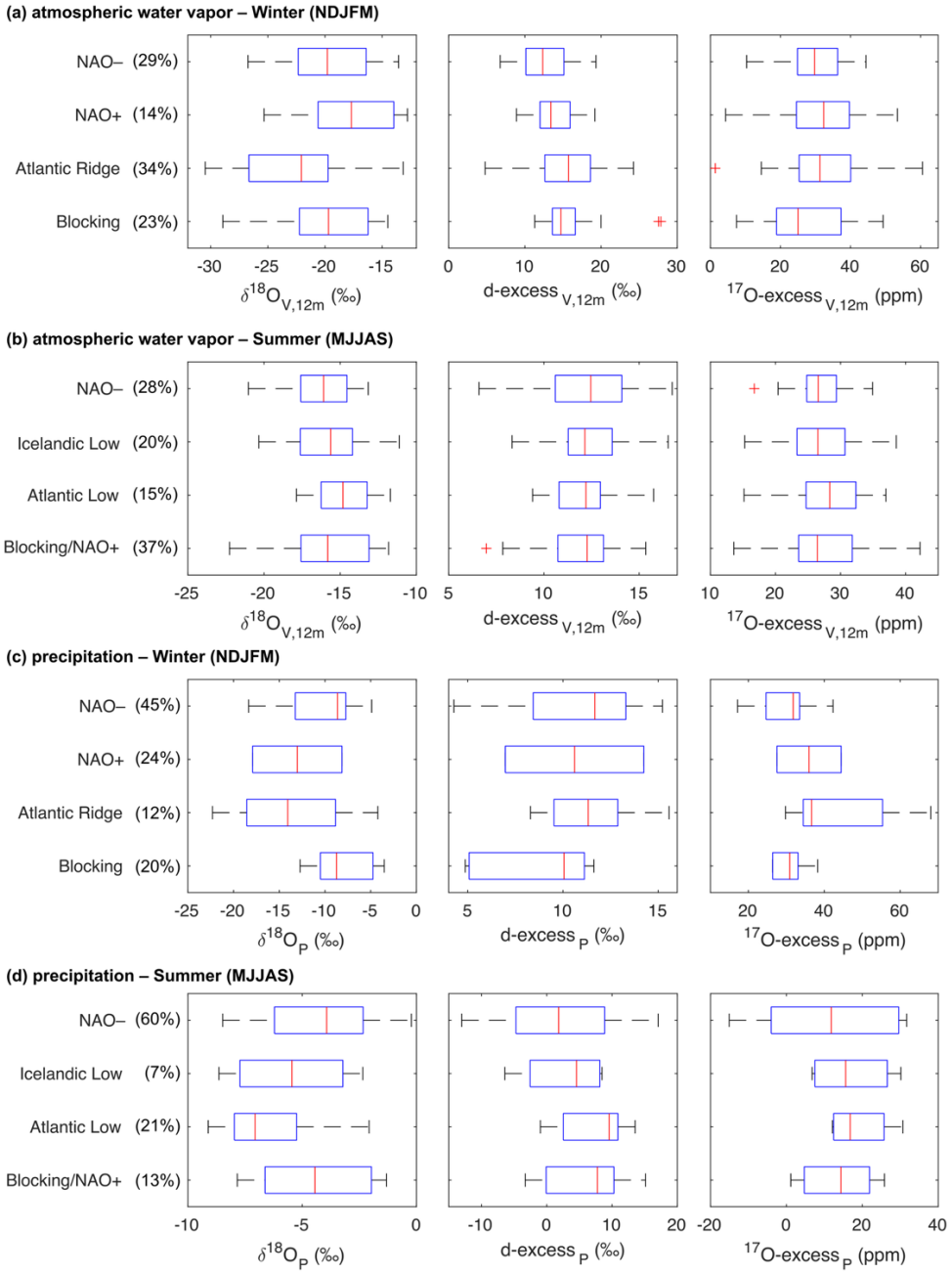

Figure C6: Box plots of isotopic compositions of (a)-(b) atmospheric water vapor and (c)-(d) precipitation for the four wintertime and the four summertime weather regimes. The red center mark indicates the median, and the lower and upper ends of the box indicate the 25th and 75th percentiles, respectively. The whiskers extend to the most extreme data points that are not considered outliers, and outliers are represented individually by the '+' marker symbol. The numbers in brackets behind the weather regime names indicate (a)-(b) the percentage of occurrence and (c)-(d) the total precipitation amount of each weather regime.

Data availability

The dataset is now available as supplementary material but will be uploaded in an online data repository after acceptance for publication. The code used for the assessment of precision of calibrated atmospheric water vapor isotopic data is available in Zenodo at: https://doi.org/10.5281/zenodo.19854015. The code used for the quantitative moisture source analysis is available in Zenodo at: https://doi.org/10.5281/zenodo.19855037.

Author contribution

CV, CVC, AA and CP designed the experiments and CV, IR, JPO and AA carried them out. CV developed the model code and performed the data analysis. FC did the statistical analysis. CC performed the classification of weather regimes. IXR provided meteorological data from the ICOS tower. CV prepared the manuscript with contributions from all co-authors.

Competing interests

The authors declare that they have no conflict of interest.

Acknowledgements

This study was conducted in the framework of the HUMI-17 project led by A.A. and supported by the ANR (ANR-17-CE01-0002-01), CNRS FR3098 ECCOREV, LABEX OT-Med, and OSU-Pytheas. It benefited from the CNRS resources allocated to the French ECOTRONS Research Infrastructure, from the Occitanie Region and FEDER investments as well as from the state allocation "Investissement d'Avenir" AnaEE-France ANR-11-INBS-0001. C.V. was supported by the Marie Curie-Sklodowska post-doctoral fellowship (#101063961).

References

Aemisegger, F., and Sjolte, J.: A climatology of strong large-scale ocean evaporation events. Part II: Relevance for the deuterium excess signature of the evaporation flux, J. Clim., 31, 7313–7336, https://doi.org/10.1175/JCLI-D-17-0592.1, 2018.

Aemisegger, F., Spiegel, J. K., Pfahl, S., Sodemann, H., Eugster, W., and Wernli, H.: Isotope meteorology of cold front passages: A case study combining observations and modelling, Geophys. Res. Lett., 42, 5652–5660, https://doi.org/10.1002/2015GL063988, 2015.

Aemisegger, F., Pfahl, S., Sodemann, H., Lehner, I., Seneviratne, S. I., and Wernli, H: Deuterium excess as a proxy for continental moisture recycling and plant transpiration, Atmos. Chem. Phys., 14, 4029–4054. https://doi.org/10.5194/acp-14-4029-2014, 2014.

Alexandre, A., Landais, A., Vallet-Coulomb, C., Piel, C., Devidal, S., Pauchet, S., Sonzogni, C., Couapel, M., Pasturel, M., Cornuault, P., Xin, J., Mazur, J. C., Prié, F., Bentaleb, I., Webb, E., Chalié, F., and Roy, J.: The triple oxygen isotope composition of phytoliths as a proxy of continental atmospheric humidity: Insights from climate chamber and climate transect calibrations, Biogeosciences, 15, 3223–3241, https://doi.org/10.5194/bg-15-3223-2018, 2018.

Alexandre, A., Webb, E., Landais, A., Piel, C., Devidal, S., Sonzogni, C., Couapel, M., Mazur, J., Pierre, M., Prié, F., Vallet-Coulomb, C., Outrequin, C., and Roy, J.: Effects of leaf length and development stage on the triple oxygen isotope signature of grass leaf water and phytoliths: insights for a proxy of continental atmospheric humidity, Biogeosciences, 16, 4613–4625, https://doi.org/10.5194/bg-16-4613-2019, 2019.

Arellano, L. N., Beverly, E. J., Voarintsoa, N. R. G., Skinner, C. B., Schauer, A. J., and Steig, E. J.: Triple oxygen isotope variability of precipitation in a tropical mountainous region, Geochim. Cosmochim. Acta, 385, 1–15, https://doi.org/10.1016/j.gca.2024.09.024, 2024.

Arnault, J., Jung, G., Haese, B., Fersch, B., Rummler, T., Wei, J., Zhang, Z., and Kunstmann, H.: A Joint Soil-Vegetation-Atmospheric Modeling Procedure of Water Isotopologues: Implementation and Application to Different Climate Zones With WRF-Hydro-Iso, J. Adv. Model. Eart Syst., 13, e2021MS002562, https://doi.org/10.1029/2021MS002562, 2021.

Aron, P. G., Levin, N. E., Beverly, E. J., Huth, T. E., Passey, B. H., Pelletier, E. M., Poulsen, C. J., Winkelstern, I. Z., and Yarian, D. A.: Triple oxygen isotopes in the water cycle, Chem. Geol., 565, 120026, https://doi.org/10.1016/j.chemgeo.2020.120026, 2021.

Baldini, L. M., McDermott, F., Foley, A. M., and Baldani, J. U. L.: Spatial variability in the European winter precipitation $\delta^{18}O$-NAO relationship: Implications for reconstructing NAO-mode climate variability in the Holocene, Geophys. Res. Lett., 35, L04709, https://doi.org/10.1029/2007GL032027, 2008.

Barkan, E., and Luz, B.: High precision measurements of $^{17}O/^{16}O$ and $^{18}O/^{16}O$ ratios in H_2O, Rapid Commun. Mass Spectrom., 19, 3737–3742, https://doi.org/10.1002/rcm.2250, 2005.

Bartsch, S., Stegehuis, A. I., Boissard, C., Lathière, J., Peterschmitt, J. Y., Reiter, I. M., Gauquelin, T., Baldy, V., Genesio, L., Matteucci, G., Fernandez, C., and Guenet, B.: Impact of precipitation, air temperature and abiotic emissions on gross primary production in Mediterranean ecosystems in Europe, Eur. J. For. Res., 139, 111–126, https://doi.org/10.1007/s10342-019-01246-7, 2020.

Bastrikov, V., Steen-Larsen, H. C., Masson-Delmotte, V., Gribanov, K., Cattani, O., Jouzel, J., and Zakharov, V.: Continuous measurements of atmospheric water vapour isotopes in western Siberia (Kourovka), Atmos. Meas. Tech., 7, 1763–1776, https://doi.org/10.5194/amt-7-1763-2014, 2014.

Berkelhammer, M., Hu, J., Bailey, A., Noone, D., Still, C. J., Barnard, H., Gochis, D., Hsiao, G. S., Rahn, T., and Turnipseed, A.: The nocturnal water cycle in an open-canopy forest, J. Geophys. Res. Atmos., 118, 10225–10242, https://doi.org/10.1002/jgrd.50701, 2013.

Bershaw, J., Penny, S. M., and Garzione, C. N.: Stable isotopes of modern water across the Himalaya and eastern Tibetan Plateau: Implications for estimates of paleoelevation and paleoclimate, J. Geophys. Res. Atmos., 117, 1-18, https://doi.org/10.1029/2011JD016132, 2012.

Bland, J. M., and Altman, D. G.: Multiple significance tests: the Bonferroni method. Br. Med. J., 310, 170. https://doi.org/10.1136/bmj.310.6973.170, 1995.

Carroll, M. L., Townshend, J. R., DiMiceli, C. M., Noojipady, P., and Sohlberg, R. A.: A new global raster water mask at 250 m resolution. Int. J. Digit. Earth, 2, 291–308, https://doi.org/10.1080/17538940902951401, 2019.

Casellas, E., Latron, J., Cayuela, C., Bech, J., Udina, M., Sola, Y., Lee, K. O., and Llorens, P.: Moisture origin and characteristics of the isotopic signature of rainfall in a Mediterranean mountain catchment (Vallcebre, eastern Pyrenees), J. Hydrol., 575, 767–779, https://doi.org/10.1016/j.jhydrol.2019.05.060, 2019.

Cassou, C.: Intraseasonal interaction between the Madden-Julian Oscillation and the North Atlantic Oscillation, Nature, 455, 523–527, https://doi.org/10.1038/nature07286, 2008.

Cassou, C., Hurrell, J. W., and Deser, C.: North Atlantic Winter Climate Regimes: Spatial Asymmetry, Stationarity with Time, and Oceanic Forcing, J. Clim., 17, 1055–1068, https://doi.org/10.1175/1520-0442(2004)017<1055:NAWCRS>2.0.CO;2, 2004.

Cassou, C., Terray, L., and Phillips, A. S.: Tropical Atlantic Influence on European Heat Waves, J. Clim., 18, 2805–2811, https://doi.org/10.1175/JCLI3506.1, 2005.

Celle-Jeanton, H., Travi, Y., and Blavoux, B.: Isotopic typology of the precipitation in the Western Mediterranean region at the three different time scales, Geophys. Res. Lett., 28, 1215–1218, https://doi.org/10.1029/2000GL012407, 2001.

Craig, H., and Gordon, L. I.: Deuterium and oxygen 18 variations in the ocean and the marine atmosphere, in: Stable Isotopes in Oceanographic Studies and Paleotemperatures, edited by: E. Tongiorgi, Consiglio Nazionale delle Ricerche Laboratorio du Geologia Nucleare, Pisa, Italy, 9–130, http://yncenter.sites.yale.edu/sites/default/files/shen_jing_jan_2013.pdf, 1965.

Cruz-San Julian, J., Araguas-Araguas, L., Rozanski, K., Benavente, J., Cardenal, J., Hidalgo, M. C., Garcia-Lopez, S., Martinez-Garrido, J. C., Moral, F., and Olias, M.: Sources of precipitation over South-Eastern Spain and groundwater recharge. An isotopic study, Tellus B, 44, 226–236, https://doi.org/10.1034/j.1600-0889.1992.t01-2-00005.x, 1992.

Dansgaard, W: Stable isotopes in precipitation, Tellus, 16, 436–468, https://doi.org/10.3402/tellusa.v16i4.8993, 1964.

Delattre, H., Vallet-Coulomb, C., and Sonzogni, C.: Deuterium excess in the atmospheric water vapour of a Mediterranean coastal wetland: regional vs. local signatures, Atmos. Chem. Phys., 15, 10167–10181, https://doi.org/10.5194/acp-15-10167-2015, 2015.

Deshpande, R. D., Maurya, A. S., Kumar, B., Sarkar, A., and Gupta, S. K.: Rain-vapor interaction and vapor source identification using stable isotopes from semiarid western India, J. Geophys. Res. Atmos., 115, D23311, https://doi.org/10.1029/2010JD014458, 2010.

Galewsky, J., Steen-Larsen, H. C., Field, R. D., Worden, J., Risi, C., and Schneider, M.: Stable isotopes in atmospheric water vapor and applications to the hydrologic cycle, Rev. Geophys., 54, 809–865, https://doi.org/10.1002/2015RG000512, 2016.

Gat, J. R.: Oxygen and Hydrogen Isotopes in the Hydrologic Cycle, Annu. Rev. Earth Planet. Sci., 24, 225–262, https://doi.org/10.1146/annurev.earth.24.1.225, 1996.

Gázquez, F., Jiménez-Espejo, F., Rodríguez-Rodríguez, M., Martegani, L., Voigt, C., Ruíz-Lara, D., Moreno, A., Valero-Garcés, B., Morellón, M., and Martín-Puertas, C.: Roman water management impacted the hydrological functioning of wetlands during drought periods, Sci. Rep., 13, 18815, https://doi.org/10.1038/s41598-023-46010-5, 2023.

Gázquez, F., Morellón, M., Bauska, T., Herwartz, D., Surma, J., Moreno, A., Staubwasser, M., Valero-Garcés, B., Delgado-Huertas, A., and Hodell, D. A.: Triple oxygen and hydrogen isotopes of gypsum hydration water for quantitative paleo-humidity reconstruction, Earth Planet. Sci. Lett., 481, 177–188, https://doi.org/10.1016/j.epsl.2017.10.020, 2018.

Giménez, R., Bartolomé, M., Gázquez, F., Iglesias, M., and Moreno, A.: Underlying Climate Controls in Triple Oxygen (^{16}O, ^{17}O, ^{18}O) and Hydrogen (^{1}H, ^{2}H) Isotopes Composition of Rainfall (Central Pyrenees), Front. Earth Sci., 9, 633698, https://doi.org/10.3389/feart.2021.633698, 2021.

Griffis, T. J., Wood, J. D., Baker, J. M., Lee, X., Xiao, K., Chen, Z., Welp, L. R., Schultz, N. M., Gorski, G., Chen, M., and Nieber, J.: Investigating the source, transport, and isotope composition of water vapor in the planetary boundary layer, Atmos. Chem. Phys., 16, 5139–5157, https://doi.org/10.5194/acp-16-5139-2016, 2016.

Graf, P., Wernli, H., Pfahl, S., and Sodemann, H.: A new interpretative framework for below-cloud effects on stable water isotopes in vapour and rain, Atmos. Chem. Phys., 19, 747–765, https://doi.org/10.5194/acp-19-747-2019, 2019.

Gröning, M., Lutz, H. O., Roller-Lutz, Z., Kralik, M., Gourcy, L., and Pöltenstein, L.: A simple rain collector preventing water re-evaporation dedicated for $\delta^{18}O$ and $\delta^{2}H$ analysis of cumulative precipitation samples, J. Hydrol., 448–449, 195–200, https://doi.org/10.1016/j.jhydrol.2012.04.041, 2012.

Guo, J., Zhang, J., Chen, T., Bai, K., Shao, J., Sun, Y., Li, N., Wu, J., Li, R., Li, J., Guo, Q., Cohen, J. B., Zhai, P., Xu, X., and Hu, F.: A merged continental planetary boundary layer height dataset based on high-resolution radiosonde measurements, ERA5 reanalysis, and GLDAS, Earth Syst. Sci. Data, 16, 1-14, https://doi.org/10.5194/essd-2022-150, 2022.

He, H., & Smith, R. B.: Stable isotope composition of water vapor in the atmospheric boundary layer above the forests of New England, J. Geophys. Res. Atmos., 104, 11657–11673, https://doi.org/10.1029/1999JD900080, 1999.

He, S., Jackisch, D., Samanta, D., Yi, P. K. Y., Liu, G., Wang, X., and Goodkin, N. F.: Understanding Tropical Convection Through Triple Oxygen Isotopes of Precipitation From the Maritime Continent, J. Geophys. Res. Atmos., 126, e2020JD033418, https://doi.org/10.1029/2020JD033418, 2021.

Hersbach, H., Bell, B., Berrisford, P., Hirahara, S., Horányi, A., Muñoz-Sabater, J., Nicolas, J., Peubey, C., Radu, R., Schepers, D., Simmons, A., Soci, C., Abdalla, S., Abellan, X., Balsamo, G., Bechtold, P., Biavati, G., Bidlot, J., Bonavita, M., … Thépaut, J. N.: The ERA5 global reanalysis, Q. J. R. Meteorol. Soc., 146, 1999–2049, https://doi.org/10.1002/qj.3803, 2020.

Huang, L., and Wen, X.: Temporal variations of atmospheric water vapor δD and $\delta^{18}O$ above an arid artificial oasis cropland in the Heihe River Basin, J. Geophys. Res. Atmos., 119, 11456–11476, https://doi.org/10.1002/2014JD021891, 2014.

IAEA/WMO: The Global Network of Isotopes in Precipitation database, https://www.iaea.org/services/networks/gnip, last access: 26 November 2025.

Koren, G., Schneider, L., van der Velde, I. R., van Schaik, E., Gromov, S. S., Adnew, G. A., Mrozek Martino, D. J., Hofmann, M. E. G., Liang, M. C., Mahata, S., Bergamaschi, P., van der Laan-Luijkx, I. T., Krol, M. C., Röckmann, T., and Peters, W.: Global 3-D Simulations of the Triple Oxygen Isotope Signature $\Delta^{17}O$ in Atmospheric CO_2, J. Geophys. Res. Atmos., 124, 8808–8836, https://doi.org/10.1029/2019JD030387, 2019.

Lai, C. T., and Ehleringer, J. R.: Deuterium excess reveals diurnal sources of water vapor in forest air, Oecologia, 165, 213–223, https://doi.org/10.1007/s00442-010-1721-2, 2011.

Landais, A., Barkan, E., and Luz, B.: Record of $\delta^{18}O$ and ^{17}O-excess in ice from Vostok Antarctica during the last 150,000 years, Geophys. Res. Lett., 35, 1–5, https://doi.org/10.1029/2007GL032096, 2008.

Landais, A., Barkan, E., Yakir, D., and Luz, B.: The triple isotopic composition of oxygen in leaf water, Geochim. Cosmochim. Acta, 70, 4105–4115, https://doi.org/10.1016/j.gca.2006.06.1545, 2006.

Landais, A., Risi, C., Bony, S., Vimeux, F., Descroix, L., Falourd, S., and Bouygues, A.: Combined measurements of $^{17}O_{excess}$ and d-excess in African monsoon precipitation: Implications for evaluating convective parameterizations, Earth Planet. Sci. Lett., 298, 104–112, https://doi.org/10.1016/j.epsl.2010.07.033, 2010.

Landais, A., Steen-Larsen, H. C., Guillevic, M., Masson-Delmotte, V., Vinther, B., and Winkler, R.: Triple isotopic composition of oxygen in surface snow and water vapor at NEEM (Greenland), Geochim. Cosmochim. Acta, 77, 304–316, https://doi.org/10.1016/j.gca.2011.11.022, 2012.

Li, S., Levin, N. E., Soderberg, K., Dennis, K. J., and Caylor, K. K.: Triple oxygen isotope composition of leaf waters in Mpala, central Kenya, Earth Planet. Sci. Lett., 468, 38–50, https://doi.org/10.1016/j.epsl.2017.02.015, 2017.

Liang, Q. S., Sha, L. J., Li, J. Y., Zhang, J., Wang, X. J., Zhou, S. L., Lin, F. Y., Xue, Y. X., Duan, R., He, Y. T., Li, H. Y., Wang, C. Y., Liu, B., Hou, Y. K., Chen, C. J., Cheng, H., and Li, T. Y.: Seasonal Variations and Controls on Triple Oxygen and Hydrogen Isotopes in Precipitation—A Case Study From Monitoring in Southwest China, J. Geophys. Res. Atmos., 129, e2023JD040654, https://doi.org/10.1029/2023JD040654, 2024.

Lin, Y., Clayton, R. N., Huang, L., Nakamura, N., and Lyons, J. R.: Oxygen isotope anomaly observed in water vapor from Alert, Canada and the implication for the stratosphere, Proc. Natl. Acad. Sci. U.S.A., 110, 15608–15613, https://doi.org/10.1073/pnas.1313014110, 2013.

Lin, Y., Wu, N., Ta, K., Landais, A., and Peng, X.: Triple Oxygen Isotopic Compositions of Ocean Water from the Mariana Trench, ACS Earth Space Chem., 5, 3087–3096, https://doi.org/10.1021/acsearthspacechem.1c00187, 2021.

Luz, B., and Barkan, E.: Variations of $^{17}O/^{16}O$ and $^{18}O/^{16}O$ in meteoric waters, Geochim. Cosmochim. Acta, 74, 6276–6286, https://doi.org/10.1016/j.gca.2010.08.016, 2010.

Majoube, M.: Fractionnement en oxygène 18 et en deutérium entre l'eau et sa vapeur, J. Chim. Phys., 68, 1423–1436, https://doi.org/10.1051/jcp/1971681423, 1971.

Mercer, J. J., Liefert, D. T., and Williams, D. G.: Atmospheric vapour and precipitation are not in isotopic equilibrium in a continental mountain environment, Hydrol. Process., 34, 3078–3101, https://doi.org/10.1002/hyp.13775, 2020.

Merlivat, L., and Jouzel, J.: Global climatic interpretation of the deuterium-oxygen 18 relationship for precipitation, J. Geophys. Res., 84, 5029–5033, https://doi.org/10.1029/JC084iC08p05029, 1979.

Michelangeli, P.-A., Vautard, R., and Legras, B.: Weather regimes: Recurrence and Quasi Stationarity. J. Atmos. Sci., 52, 1237–1256, https://doi.org/10.1175/1520-0469(1995)052%3C1237:WRRAQS%3E2.0.CO;2, 1995.

NASA/GES DISC, GLDAS Land/Sea Mask Dataset, 1° resolution, Global Land Data Assimilation System (GLDAS), based on MOD44W MODIS water mask (Carroll et al. 2009), available at: https://ldas.gsfc.nasa.gov/gldas/vegetation-class-mask (accessed: 19 March 2026).

Natali, S., Doveri, M., Giannecchini, R., Baneschi, I., and Zanchetta, G.: Is the deuterium excess in precipitation a reliable tracer of moisture sources and water resources fate in the western Mediterranean? New insights from Apuan Alps (Italy), J. Hydrol., 614, 128497, https://doi.org/10.1016/j.jhydrol.2022.128497, 2022.

Natali, S., Baneschi, I., Doveri, M., Giannecchini, R., Selmo, E., and Zanchetta, G.: Meteorological and geographical control on stable isotopic signature of precipitation in a western Mediterranean area (Tuscany, Italy): Disentangling a complex signal, J. Hydrol., 603, 126944, https://doi.org/10.1016/j.jhydrol.2021.126944, 2021.

Obermann, A., Bastin, S., Belamari, S., Conte, D., Gaertner, M. A., Li, L., and Ahrens, B.: Mistral and Tramontane wind speed and wind direction patterns in regional climate simulations, Clim. Dyn., 51, 1059–1076, https://doi.org/10.1007/s00382-016-3053-3, 2018.

Outrequin, C., Alexandre, A., Vallet-Coulomb, C., Piel, C., Devidal, S., Landais, A., Couapel, M., Mazur, J., Peugeot, C., Pierre, M., Prié, F., Roy, J., Sonzogni, C., and Voigt, C.: The triple oxygen isotope composition of phytoliths, a new proxy of atmospheric relative humidity: controls of soil water isotope composition, temperature, CO_2 concentration and relative humidity, Clim. Past, 17, 1881–1902, https://doi.org/10.5194/cp-17-1881-2021, 2021.

Penchenat, T., Vimeux, F., Daux, V., Cattani, O., Viale, M., Villalba, R., Srur, A., and Outrequin, C.: Isotopic Equilibrium Between Precipitation and Water Vapor in Northern Patagonia and Its Consequences on $\delta^{18}O_{cellulose}$ Estimate, J. Geophys. Res. Biogeosci., 125, e2019JG005418, https://doi.org/10.1029/2019JG005418, 2020.

Pfahl, S., and Wernli, H.: Air parcel trajectory analysis of stable isotopes in water vapor in the eastern Mediterranean, J. Geophys. Res. Atmos., 113, 1–16, https://doi.org/10.1029/2008JD009839, 2008.

Pierchala, A., Rozanski, K., Dulinski, M., and Gorczyca, Z.: Triple-isotope mass balance of mid-latitude, groundwater controlled lake, Sci. Total Environ., 814, 151935, https://doi.org/10.1016/j.scitotenv.2021.151935, 2021.

Ranjan, S., Ramanathan, A. L., Keesari, T., Singh, V. B., Kumar, N., Pandey, M., and Leuenberger, M. C.: Triple Water Vapour–Isotopologues Record from Chhota Shigri, Western Himalaya, India: A Unified Interpretation based on $\delta^{17}O$, $\delta^{18}O$, δD and Comparison to Meteorological Parameters, Front. Earth Sci., 8, 1–16, https://doi.org/10.3389/feart.2020.599632, 2021.

Reiter, I. M., Castagnoli, G., and Rotereau, A.: COOPERATE database [dataset]. https://cooperate.eccorev.fr/db, 2015.

Rothfuss, Y., Quade, M., Brüggemann, N., Graf, A., and Vereecken, H.: Reviews and syntheses: Gaining insights into evapotranspiration partitioning with novel isotopic monitoring methods, Biogeosciences, 18, 3701–3732, https://doi.org/10.5194/bg-18-3701-2021, 2021.

Risi, C., Noone, D., Worden, J., Frankenberg, C., Stiller, G., Kiefer, M., Funke, B., Walker, K., Bernath, P., Schneider, M., Bony, S., Lee, J., Brown, D., and Sturm, C.: Process-evaluation of tropospheric humidity simulated by general circulation models using water vapor isotopic observations: 2. Using isotopic diagnostics to understand the mid and upper tropospheric moist bias in the tropics and subtropics, J. Geophys. Res. Atmos., 117, D05304, https://doi.org/10.1029/2011JD016623, 2012.

Rozanski, K., Araguás-Araguás, L., and Gonfiantini, R.: Isotopic Patterns in Modern Global Precipitation, in: Climate Change in Continental Isotopic Records, edited by: Swart, K., Lohmann, K.C., Mckenzie, J. and Savin, S., 78, 1–36, https://doi.org/10.1029/gm078p0001, 1993.

Saighi, O.: Isotopic composition of precipitation from Algiers and Assekrem, in: Isotopic composition of precipitation in the Mediterranean Basin in relation to air circulation patterns and climate: final report of a coordinated research project, 2000-2004, edited by: International Atomic Energy Agency, Vienna, Austria, 5–17, ISBN 92–0–105305–3, 2005.

Salmon, O., Welp, L. R., Baldwin, M., Hajny, K., Stirm, B., and Shepson, P.: Vertical profile observations of water vapor deuterium excess in the lower troposphere, Atmos. Chem. Phys., 19, 11525–11543, https://doi.org/10.5194/acp-19-11525-2019, 2019.

Sharp, Z. D., Wostbrock, J. A. G., and Pack, A.: Mass-dependent triple oxygen isotope variations in terrestrial materials, Geochem. Perspect. Lett., 7, 27–31, https://doi.org/10.7185/geochemlet.1815, 2018.

Simonin, K. A., Link, P., Rempe, D., Miller, S., Oshun, J., Bode, C., Dietrich, W. E., Fung, I., and Dawson, T. E.: Vegetation induced changes in the stable isotope composition of near surface humidity, Ecohydrology, 7, 936–949, https://doi.org/10.1002/eco.1420, 2014.

Sodemann, H., Schwierz, C., and Wernli, H.: Interannual variability of Greenland winter precipitation sources: Lagrangian moisture diagnostic and North Atlantic Oscillation influence, J. Geophys. Res. Atmos., 113, 1–17, https://doi.org/10.1029/2007JD008503, 2008.

Sodemann, H., Aemisegger, F., Pfahl, S., Bitter, M., Corsmeier, U., Feuerle, T., Graf, P., Hankers, R., Hsiao, G., Schulz, H., Wieser, A., and Wernli, H.: The stable isotopic composition of water vapour above Corsica during the HyMeX SOP1 campaign: Insight into vertical mixing processes from lower-tropospheric survey flights, Atmos. Chem.Phys., 17, 6125–6151, https://doi.org/10.5194/acp-17-6125-2017, 2017.

Stein, A. F., Draxler, R. R., Rolph, G. D., Stunder, B. J. B., Cohen, M. D., and Ngan, F.: NOAA's HYSPLIT atmospheric transport and dispersion modeling system, Bull. Am. Meteorol. Soc., 96, 2059–2077, https://doi.org/10.1175/BAMS-D-14-00110.1, 2015.

Surma, J., Assonov, S., Bolourchi, M. J., and Staubwasser, M.: Triple oxygen isotope signatures in evaporated water bodies from the Sistan Oasis, Iran, Geophys. Res. Lett., 42, 8456–8462, https://doi.org/10.1002/2015GL066475, 2015.

Surma, J., Assonov, S., Herwartz, D., Voigt, C., and Staubwasser, M.: The evolution of ^{17}O-excess in surface water of the arid environment during recharge and evaporation, Sci. Rep., 8, 1–10, https://doi.org/10.1038/s41598-018-23151-6, 2018.

Surma, J., Assonov, S., and Staubwasser, M.: Triple Oxygen Isotope Systematics in the Hydrologic Cycle, Rev. Mineral. Geochem., 86, 401–428, https://doi.org/10.2138/rmg.2021.86.12, 2021.

Tada, M., Yoshimura, K., and Toride, K.: Improving weather forecasting by assimilation of water vapor isotopes, Sci. Rep., 11, 18067, https://doi.org/10.1038/s41598-021-97476-0, 2021.

Terzer-Wassmuth, S., Araguás-Araguás, L. J., Wassenaar, L. I., and Stumpp, C.: Global and local meteoric water lines for $\delta^{17}O/\delta^{18}O$ and the spatiotemporal distribution of $\Delta'^{17}O$ in Earth's precipitation, Sci. Rep., 13, 19056, https://doi.org/10.1038/s41598-023-45920-8, 2023.

Tremoy, G., Vimeux, F., Soumana, S., Souley, I., Risi, C., Favreau, G., and Oï, M.: Clustering mesoscale convective systems with laser-based water vapor $\delta^{18}O$ monitoring in niamey (Niger). J. Geophys. Res., 119, 5079–5103, https://doi.org/10.1002/2013JD020968, 2014.

Tsujimura, M., Sasaki, L., Yamanaka, T., Sugimoto, A., Li, S. G., Matsushima, D., Kotani, A., and Saandar, M.: Vertical distribution of stable isotopic composition in atmospheric water vapor and subsurface water in grassland and forest sites, eastern Mongolia, J. Hydrol., 333, 35–46. https://doi.org/10.1016/j.jhydrol.2006.07.025, 2007.

Uemura, R., Barkan, E., Abe, O., and Luz, B.: Triple isotope composition of oxygen in atmospheric water vapor, Geophys. Res. Lett., 37, 1–4, https://doi.org/10.1029/2009GL041960, 2010.

Vallet-Coulomb, C., Couapel, M., and Sonzogni, C.: Improving memory effect correction to achieve high precision analysis of $\delta^{17}O$, $\delta^{18}O$ $\delta^{2}H$, ^{17}O-excess and d-excess in water using cavity ring-down laser spectroscopy, Rapid Commun. Mass Spectrom., 35, e9108, https://doi.org/10.1002/rcm.9108, 2021.

Vautard, R.: Multiple weather regimes over the North Atlantic: Analysis of Precursors and Successors, Mon. Weather Rev., 118, 2056–2081, https://doi.org/10.1175/1520-0493(1990)118%3C2056:MWROTN%3E2.0.CO;2, 1990.

Voarintsoa, N. R. G.: A 3.5-year rainfall isotope records from northwestern Madagascar featuring $^{17}O_{excess}$ and implication for paleoclimate research, Appl. Geochem., 184, 106335, https://doi.org/10.1016/j.apgeochem.2025.106335, 2025.

Voigt, C., Alexandre, A., Reiter, I. M., Orts, J. P., Vallet-Coulomb, C., Piel, C., Mazur, J. C., Aleman, J. C., Sonzogni, C., Miche, H., and Ogée, J.: Examination of the parameters controlling the triple oxygen isotope composition of grass leaf water and phytoliths at a Mediterranean site: a model-data approach, Biogeosciences, 20, 2161–2187, https://doi.org/10.5194/bg-20-2161-2023, 2023.

Voigt, C., Gázquez, F., Martegani, L., Sánchez Villanueva, A. I., Medina, A., Jiménez-Espinosa, R., Jiménez-Millán, J., and Rodríguez-Rodríguez, M.: How seasonal hydroclimate variability drives the triple oxygen and hydrogen isotope composition of small lake systems in semiarid environments, Hydrol. Earth Syst. Sci., 29, 1783-1806, https://doi.org/10.5194/hess-29-1783-2025, 2025.

Voigt, C., Herwartz, D., Dorador, C., and Staubwasser, M.: Triple oxygen isotope systematics of evaporation and mixing processes in a dynamic desert lake system, Hydrol. Earth Syst. Sci., 25, 1211–1228, https://doi.org/10.5194/hess-25-1211-2021, 2021.

waterisotopes-CISE-LOCEAN: Water isotopes of sea water analyzed since 1998 at LOCEAN, SEANOE [dataset], https://doi.org/https://doi.org/10.17882/71186, 2025.

Wen, X. F., Zhang, S. C., Sun, X., Yu, G., and Lee, X.: Water vapor and precipitation isotope ratios in Beijing, China, J. Geophys. Res. Atmos., 115, D01103, 1–10, https://doi.org/10.1029/2009JD012408, 2010.

Welp, L. R., Lee, X., Griffis, T. J., Wen, X. F., Xiao, W., Li, S., Sun, X., Hu, Z., Val Martin, M., and Huang, J.: A meta-analysis of water vapor deuterium-excess in the midlatitude atmospheric surface layer, Global Biogeochem. Cycles, 26, 1–12, https://doi.org/10.1029/2011GB004246, 2012.

Xia, Z., Surma, J., and Winnick, M. J.: The response and sensitivity of deuterium and ^{17}O-excess parameters in precipitation to hydroclimate processes, Earth-Sci. Rev., 242, 104432, https://doi.org/10.1016/j.earscirev.2023.104432, 2023.

Xia, Z., Welker, J. M., and Winnick, M. J.: The Seasonality of Deuterium Excess in Non-Polar Precipitation, Global Biogeochem. Cycles, 36, e2021GB007245, https://doi.org/10.1029/2021GB007245, 2022.

Zhang, Y., Legrande, A. N., Goodkin, N., Nusbaumer, J., He, S., Schmidt, G. A., and Wang, X.: Exploring Precipitation Triple Oxygen Isotope Dynamics: Insights from GISS-E2.1 Simulations, J. Adv. Model. Earth Syst., 17, e2024MS004509, https://doi.org/10.1029/2024MS004509, 2025.

Zhao, L., Wang, L., Liu, X., Xiao, H., Ruan, Y., & Zhou, M.: The patterns and implications of diurnal variations in the d-excess of plant water, shallow soil water and air moisture, Hydrol. Earth Syst. Sci., 18, 4129–4151, https://doi.org/10.5194/hess-18-4129-2014, 2014.